PCCP

Accepted Manuscript

ROYAL SOCIETY OF CHEMISTRY

www.rsc.org/pccp

Journal Name

ARTICLE TYPE

Cite this: DOI: 10.1039/xxxxxxxxxx

Energy level modeling of lanthanide materials: review and uncertainty analysis†

Jonas J. Joos, Dirk Poelman, and Philippe F. Smet

Received Date
Accepted Date

DOI: 10.1039/xxxxxxxxxx

www.rsc.org/journalname

Energy level schemes are an essential tool for the description and interpretation of atomic spectra. During the last 40 years, several empirical methods and relationships were devised for constructing energy level schemes of lanthanide defects in wide band gap solids, culminating in the chemical shift model by Thiel and Dorenbos. This model allows to calculate the electronic and optical properties of the considered materials. However, an unbiased assessment of the accuracy of the obtained values of the calculated parameters is still lacking to a large extent. In this paper, error margins for calculated electronic and optical properties are deduced. It is found that optical transitions can be predicted within an acceptable error margin, while the description of phenomena involving conduction band states is limited to qualitative interpretation due to the large error margins for physical observables such as thermal quenching temperature, corresponding with standard deviations in the range 0.3-0.5 eV for the relevant energy differences. As an example, the electronic structure of lanthanide doped calcium thiogallate ($CaGa_2S_4$) is determined, taking the experimental spectra of $CaGa_2S_4$:Ln^{Q+} (Ln^{Q+} = Ce^{3+}, Eu^{2+}, Tm^{3+}) as input. Two different approaches to obtain the shape of the zig-zag curves connecting the 4f levels of the different lanthanides are explored and compared.

1 Introduction

Luminescent materials are ubiquitous in todays technology driven society. Phosphors, i.e. color converting materials, are key components in white light-emitting diodes (LEDs), the most promising technology for lighting[1–7]. Furthermore, white LEDs are very important in modern displays, e.g. making up the backlight unit in liquid crystal displays (LCD)[8,9]. Solid state lasers based on lanthanide or transition metal doped crystals, with their emission ranging from infrared to ultraviolet, form a huge and important application domain, e.g. in telecommunication[10]. Scintillators and storage phosphors serve in radiation detection in general and medical imaging in particular[11–14]. Luminescent materials exhibiting temperature or pressure dependent properties can be used for contactless thermography or pressure sensing[15–19]. Glow-in-the-dark or persistent luminescent materials get established in emergency signalization, medical imaging and decoration[20–23].

The growing demand towards more specialized materials raises new challenges for science and materials engineering. More than before, a theoretical framework is required to design materials on the drawing board before actual synthesis. Quantitative theoretical description of the spectra of metal ions dates from the 1930s when crystal field theory was devised[24,25]. Since then, a lot of progress has been made and nowadays different complementary approaches can be found in literature.

In *ab initio* or first principles calculations, a quantum mechanical framework is used to calculate and understand the correlation between the structure and functionality of materials. For luminescent properties, a correct description of both the electronic ground and excited states is essential. This proves to be a very difficult exercise for standard *ab initio* techniques in the case of unfilled d and f shells of metal ions because of their complex electronic structure, electron correlation effects and the presence of relativistic effects[26]. Nonetheless, interesting results from *ab initio* calculations were reported. Multireference wavefunction based techniques have proven to yield insights into the excited state dynamics underlying electronic spectroscopy, see for example[27–34].

Density functional theory (DFT) based techniques are becom-

LumiLab, Department of Solid State Sciences, Ghent University, Ghent, Belgium; E-mail: philippe.smet@UGent.be
Center for Nano- and Biophotonics (NB Photonics), Ghent University, Ghent, Belgium.

† Electronic Supplementary Information (ESI) available: 1. Illustrative cartoon on how an energy level scheme is constructed from the calculated quantities. 2. Table of $4f^N$-$4f^{N-1}6s^1$ transition energies for free lanthanide ions. See DOI: 10.1039/b000000x/

ing a more popular tool, though multiplets as they are found in spectroscopic experiments do not straightforwardly emerge from the calculations[35]. Within the semi-empirical Kohn-Sham DFT scheme multiple worthwhile results are available in literature. Canning et al. successfully described the luminescent properties of a multitude of scintillators, based on the Ce^{3+} and Eu^{2+} ions within the DFT+U formalism[36–38]. In so-called ligand field DFT (LFDFT), an averaging of the considered electronic configuration is performed on the Kohn-Sham orbitals, allowing to calculate atomic-like Racah and crystal field parameters[39–44]. Multiple alternative computational techniques are still under development[45–47].

Although advances in quantum mechanical calculations are promising, a vast amount of computer power and user experience is necessary to yield trustworthy results. Empirical models on the other hand lack the formal theoretical basis of *ab initio* techniques, but allow for fast and computationally simple prediction of optical properties. Empirical relationships and rules of thumb pertaining to lanthanide materials have been reported during the last 40 years by multiple authors. During the last 20 years, Dorenbos excavated many of these relationships and observations from literature and tested them to a vast amount of experimental data, both confirming the correctness of existing models and rules, as well as uncovering new relationships[48]. Rather than being rooted in a strong physical description, these models are empirical in nature, as they are constructed from a large amount of experimental data or parameters and subsequent fitting. Models are thus statistical in nature and predictions about yet to be performed experiments are essentially an extrapolation of existing data. However, interpretation of the empirical laws in terms of more fundamental physical laws is sometimes possible, but even then it remains usually necessary to introduce empirical parameters.

If a theory or a model allows to predict observable quantities, it should also be possible to get a grasp of the error margins associated with the model and consequently of the accuracy of the calculated parameters. This paper aims to give an overview of the errors, which are statistical in nature, being inherent to the calculation of electronic and optical properties by the conventional empirical relationships.

These empirical relationships are further explored to construct energy level schemes of lanthanide doped $CaGa_2S_4$ phosphors. This ternary sulfide is well known as host crystal for efficient lanthanide luminescence. It is therefore a suitable test case based on the detailed description in literature[49–53]. An empirical host referred binding energy level scheme was already constructed in 2005, although some radical simplifications were made at that time[53]. Relevant quantities, describing the optical and electronic properties of $CaGa_2S_4$:Ln^{Q+} materials are calculated and the error margins assessed, based on the prior error analysis.

This text is organized in two parts that are written from two different point of views. In the first part (§3), the electronic structure of metal impurities with an unfilled d or f shell inside semiconducting or insulating materials is discussed in a general and qualitative way. The purpose of this part is to appreciate the different available (semi-) empirical approaches in their broader theoretical context. Common difficulties in the interpretation of the empirical models are addressed. The second part (§4-7) focuses on empirical energy level modeling. A step-by-step guide is presented on how empirical energy level schemes can be obtained starting from limited experimental input, supplemented by an uncertainty analysis which does not only assess the errors on the energy level locations, but also - more important - on the derived experimental quantities (§4). A section (§5) is devoted on how the required experimental parameters can be obtained through spectroscopy. The empirical energy level models and the uncertainty analysis are finally applied on the $CaGa_2S_4$:Ln^{Q+} systems (§7).

2 Experimental

$CaGa_2S_4$:Ln^{Q+} powders were synthesized by a solid state reaction at high temperature (2 hours at 900°C, heating rate of 7.5°C/min) under a flux of forming gas (90% N_2, 10% H_2). CaS (Alfa Aesar, 99.9%) and Ga_2S_3 (Alfa Aesar, 99.99%) were used as starting materials for the host crystal and lanthanide fluorides (LnF_3, all at least 99.5% pure) as source of the dopants. $CaGa_2S_4$ was doped with Ce, Eu and Tm. A doping concentration of 1 mol% was used for all syntheses. The phase purity of the obtained powders was verified by means of X-ray diffraction (XRD) with Cu$K\alpha_1$ radiation on a Bruker D5000 diffractometer. Luminescence emission and excitation spectra were measured with an Edinburgh FS920 fluorescence spectrometer. Spectra at 75 K were obtained by using an Oxford Optistat CF cryostat. Diffuse reflectance spectra were measured with a Varian Cary 500 spectrophotometer, equipped with an internal 110 mm $BaSO_4$-coated integrating sphere.

3 Atomic versus band picture of optical dopants

In literature, energy level schemes of lanthanide and transition metal impurities in semiconductors or wide band gap solid are described in two different ways. Both points of view are briefly reviewed here and the formal connection between them is examined, to avoid possible confusion.

On the one hand, the so-called crystal field theory (CFT) assumes that the electronic structure of the free metal ion is only weakly altered by the surrounding crystal. This allows a description of the electronic eigenstates in atomic-like many-particle basis functions, labeled by many-particle quantum numbers such as total angular momenta. The fundamental idea of this approach dates from the 1920-30's and is attributed to Bethe and Van Vleck[24,25]. In CFT, an effective hamiltonian, describing the electron shell under consideration, is diagonalized. The matrix elements of the hamiltonian can be obtained by separating the angular dependent part - which is exactly computable due to the

Wigner-Eckart theorem and Racah's irreducible tensor algebra - from the radial dependent part for which no straightforward analytical expression exists and should therefore be obtained from experiments or *ab initio* calculations[54–57]. The CFT approach has been specifically successful in describing interconfigurational $4f^N$ transitions in lanthanide ions and interconfigurational $3d^N$ transitions in transition metal ions. Though very high accuracies can be obtained with this technique, corresponding with standard deviations* of a few meV for $4f^N$ manifolds, this comes at the risk of over-parameterization as a lot of radial integrals are required in the effective hamiltonian. In the last decade, CFT has been extended for describing $nf^{N-1}(n+1)d^1$ manifolds of lanthanide and actinide ions. This can be done with standard deviations in the range of 10-100 meV[58–61]. As an atomic basis is employed, it is not possible to describe charge transfer transitions within this framework.

On the other hand, the electronic structure of the dopant can be described in terms of localized defect levels introduced in the host's band structure, behaving as deep donors/acceptors or recombination centers. The idea that the unfilled d shell of transition metal ions is responsible for deep levels dates from the 1960s and is due to Allen[62]. The basis describing the electronic eigenstates in this case are of a single particle nature, i.e. Bloch or Wannier states[63–67]. Energy level schemes in terms of these noninteracting particles consist of a Fermi sea of occupied states, separated by the Fermi level from the unoccupied single particle states at higher energy, at least at absolute zero. This is the conventional picture of a semiconductor[65,67,68]. Although this approach has been successful in describing isoelectronic substitutional impurities in semiconductors, the independent particle picture does not allow to describe the many-body effects which cannot be ignored for the highly correlated electrons in the impurity's d and f shells† [69,70]. Ligand field theory, which is often used to describe the electronic structure of metal ion complexes can be regarded in the same way since the molecular orbitals likewise represent single particle orbitals.

Both approaches are demonstrated for the case of the Pr^{3+} ion. In Fig. 1a, the perturbed atomic-like states of the ion are shown. Energies of interconfigurational $4f^2$ and intraconfigurational 4f5d transitions can be immediately read from this many-particle scheme by subtracting the total energies of final and initial states. The energy shown represents the total energy of the two electrons involved, with respect to the $4f^2$ ground state.

In Fig. 1b, the superposition of the host's valence and conduction bands and the single particle impurity levels of the Pr^{3+} dopant are shown. Electronic transitions in this type of energy level scheme are straightforward to imagine as a particle-hole excitation for which the energy is simply the difference in orbital energy between the particle and hole states in accordance with Koopmans' theorem‡.

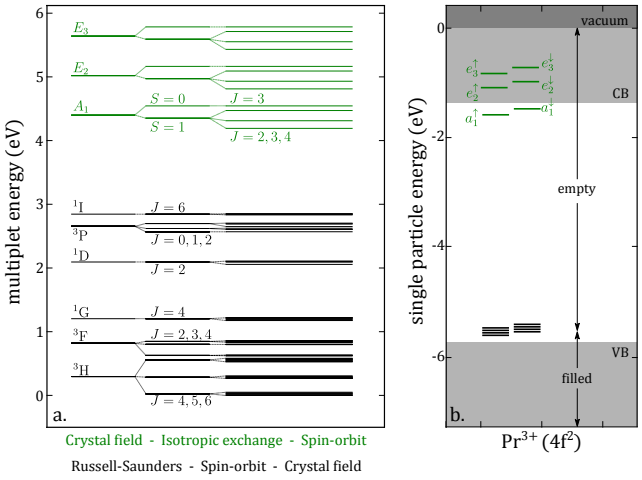

Fig. 1 Illustration of the atomic and band pictures for a fictive Pr^{3+} defect on a site with D_{4d} symmetry. a. The multiplets corresponding with the $4f^2$ and 4f5d configurations are shown as obtained with conventional crystal field theory (in respectively the $\left|4f^{2\ 2S+1}L_J(\Gamma)\right\rangle$ and $\left|\left[4f(^2F),\ 5d\,(^2\Gamma)\right]SJ\right\rangle$ basis). b. The energy levels of a spin-polarized Hartree-Fock calculation are shown, describing the Pr defect in terms of single particle orbitals. The shaded band represent the unbound states (vacuum), valence (VB) and conduction bands (CB)[62,71].

The two types of energy level scheme represent different physical quantities, i.e. total energies of interacting electrons and single particle energies respectively. For this reason, it can be ambiguous to simultaneously apply both approaches or even devise hybrid types of energy level schemes which are likely to be meaningless. The reason for the existence of two completely different theories is the dual nature of the optical spectra of transition metal and lanthanide ions, reflecting interatomic as well as intra-atomic transitions.

Notwithstanding the ambiguities, a unified theoretical approach is possible if the hybridization of the Bloch states for the host electron with the f and d states of the impurity is correctly described in addition to the electron correlation in the unfilled shells. The foundation for this description was laid in 1976 by extending the Anderson impurity model for metals to the case of semiconductors[69,70]. The procedure to arrive at this solution is briefly reviewed. For a detailed account, the reader is directed to the book of Kikoin and Fleurov[62].

Firstly, the single particle states ought to be accommodated for hybridization with the states of the host. This is obtained by

* In CFT, the standard deviation is conventionally defined as $\sqrt{\frac{\Sigma_i\left(E_i^{\mathrm{exp}}-E_i^{\mathrm{calc}}\right)}{N-P}}$ for N levels of a manifold, using P empirical parameters in the CF calculation[56].

† Formally, the correlation energy is defined as the difference between the Hartree-Fock energy and the *exact* total energy of a system. It is due to the two-electron (Coulomb) interactions that are not accounted for in a mean field theory. Especially static correlation, which works at long range is important for f electron systems[26].

‡ Koopmans theorem states that the removal energy of an electron corresponds to the Hartree-Fock single particle energy[72,73]

treating the central field of the impurity atom and the host's mean field together with the interaction potential between dopant and host electrons - which allows for resonant scattering - in a self-consistent way. The single particle basis used is composed of both Bloch states and impurity centered f or d functions. This treatment results in a deformation of the f and d functions which remain labeled by the irreducible representations of the point group corresponding with the site symmetry, γ. The nature of this orbital deformation will be different for each label γ, depending on the orientation of the orbital with respect to the neighboring atoms. This covalent hybridization thus causes the orbitals to have a different radial component for each label γ, additional to the different angular components which are already accounted for in conventional crystal field theory. Secondly, these altered orbitals can be coupled according to the standard procedure to obtain the many-body basis in which the electronic eigenstates are described. This particular description of the impurity ion is referred to as the pseudo-atom or pseudo-ion [62,69–71,74,75].

Once the many-particle basis of the pseudo-ion is available, the remaining interactions - i.e. the non-spherical symmetric part of the electronic Coulomb repulsion and spin-orbit interactions - are treated perturbatively as in conventional CFT, resulting in the final many-body eigenstates and eigenvalues. Due to the covalent renormalization, more Racah parameters are required than in conventional CFT. This modification is called the multiplicity correction. The effect of covalency is accounted for in an averaged change of the free ion Racah parameters in conventional CFT where it is called the nephelauxetic effect [62,75].

In the case of the 4f levels of lanthanides, the correlation effect dominates the covalency effect amply due to the localized and shielded nature of these electrons. In the case of the 5d levels of lanthanides or the 3d levels of first row transition metals, covalency is equally important [62,76,77].

Within this more general theory, both interatomic and intra-atomic transitions are properly described. For example in the case of a charge transfer (CT) transition in which a valence electron is added to the ℓ shell of a metal impurity, altering its formal charge ($\ell^N + e_V \rightarrow \ell^{N+1}$) [62,75]:

$$E^{\mathrm{CT}} = E_{\Psi_f^{N+1}}(\ell^{N+1}) + E_{\mathrm{band}}(N_V - 1) - E_{\Psi_i^N}(\ell^N) - E_{\mathrm{band}}(N_V) \quad (1)$$

where E_{Ψ^N} is the total energy of the many-body eigenstate Ψ^N and $E_{\mathrm{band}}(N_V)$ is the total energy of the N_V electrons in the valence band. As one can see, $E^{\mathrm{CT}}(\mathrm{Ln}^{3+})$ does not correspond to the mere difference in one particle energies due to electron correlation in the unfilled shell ($E_{\Psi_f}(\ell^{N+1}) - E_{\Psi_i}(\ell^N) \neq E_{\gamma_f} - E_{\gamma_i}$) as well as the change in resonant impurity scattering for different occupations of the unfilled shell ($E_{\mathrm{band}}(N_V) \neq E_{\mathrm{band}}(N_V - 1)$). Koopmans' theorem is therefore violated in real situations where wave functions do change upon quasiparticle excitation [62,73,75]. Now, an improvement of the multiplet energy level scheme of Fig. 1a can be devised, allowing for intra-atomic transitions in addition to interatomic transitions. The idea is to measure the

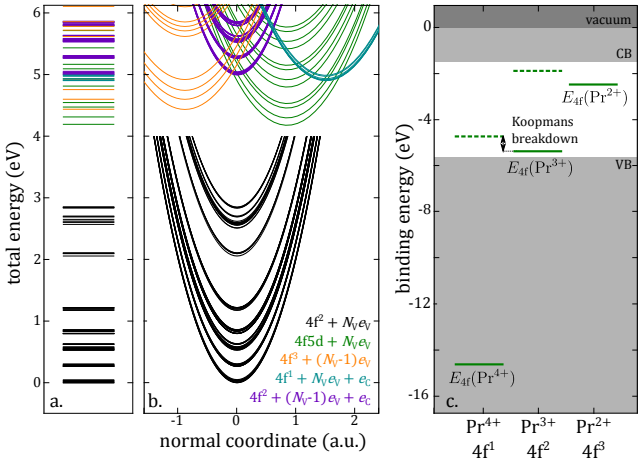

Fig. 2 a. Hypothetical energy level scheme, displaying the total energy of the electrons in the Pr pseudo-ion and in the host's valence and conduction bands. b. Configuration coordinate diagram displaying the total energy as a function of the nuclear coordinates. c. Projection of the many-body multiplets of the Pr pseudo-ion on the single-electron band scheme for the different charge states of the defect. The *virtual* 4f orbital corresponds to the charge-state transition energy if Koopmans' theorem would be valid and is represented by a dashed line. The real thermodynamic charge-state transition energies are given by the solid lines.

total energy of *all* interacting electrons in the system, not merely the electrons in the unfilled shells. An example is given in Fig. 2a. In Fig. 2b, the corresponding configuration coordinate diagram is displayed, accounting for the effect of relaxation of the nuclear coordinates because of the changing electronic configuration.

As single-particle levels do not have a meaning for correlated systems, a clear definition is required for the binding energy of the unfilled shell with respect to the host's bands. For this reason, the thermodynamic charge-state transition levels, $E_{n\ell}(Q, Q+1)$, are introduced, being the chemical potential[§] for the electrons of the system at which the defect undergoes a valence change by adding or removing an electron in the $n\ell$ shell [77–79]. The experimental significance of this level is that for chemical potentials above $E_{n\ell}(Q, Q+1)$, the defect in charge state Q is stable, while for chemical potentials below $E_{n\ell}(Q, Q+1)$, the charge state $Q+1$ is stable. Thermodynamic transition levels correspond to thermal ionization energies where a slow reorganization of the nuclear positions is possible and are therefore independent on the direction in which the electron transfer occurs [79]. In the case of optically induced charge transfers the nuclei are frozen on the timescale of the transition. Therefore, adding an electron shifts the corresponding level to higher energies, $E^{\mathrm{opt}}_{n\ell}(Q+1 \rightarrow Q) > E_{n\ell}(Q, Q+1)$, while removing an electron shifts it to lower energies, $E^{\mathrm{opt}}_{n\ell}(Q \rightarrow Q+1) < E_{n\ell}(Q, Q+1)$ [79].

One could identify the thermodynamic charge-state transition level with a Hartree-Fock single-particle level, assuming validity of the Koopmans' theorem. However, due to the covalent

§ At absolute zero, the chemical potential is referred to as the Fermi level.

renormalization and the electron correlation, this theorem breaks down and different thermodynamic charge-state transition levels are found for the different charge states. This is demonstrated in Fig. 2c. Herein, $n\ell = 4\mathrm{f}$ and the notation $E_{4\mathrm{f}}(\mathrm{Ln}^{Q+})$ is introduced to represent $E_{4\mathrm{f}}(Q, Q+1)$.

In the remainder of this review, empirical rules are surveyed which allow to construct energy level schemes of type Fig. 2c for divalent and trivalent lanthanide defects. Charge-state transition levels are simply referred to as 4f levels or 4f states in the present case of lanthanide defects.

4 Review and error calculation of empirical energy level modeling

When vacuum referred energy level schemes are constructed, the chemical shift, $E_{4\mathrm{f}}^{\mathrm{chem}}(\mathrm{Ln}^{Q+}, A)$, is the first parameter to be determined. This refers to the shift of the 4f state of a lanthanide ion ($E_{4\mathrm{f}}$) with respect to the vacuum level, i.e. the ionization potential, upon incorporation of the ion in a given host A (or more specifically: on a given lattice site (see §5.6)):

$$E_{4\mathrm{f}}(\mathrm{Ln}^{\mathrm{Q}+}, \mathrm{A}) = \mathrm{E}_{4\mathrm{f}}(\mathrm{Ln}^{\mathrm{Q}+}, \mathrm{free}) + \mathrm{E}_{4\mathrm{f}}^{\mathrm{chem}}(\mathrm{Ln}^{\mathrm{Q}+}, \mathrm{A}). \qquad (2)$$

The notion of chemical shift was first introduced by Pauling in 1929 for alkali halides[80]. It was revived by Pedrini et al. in 1978 to describe the photoconductivity threshold of divalent lanthanide impurities in alkaline earth fluorides[81–83]. In 2001, Thiel constructed a complete vacuum referred lanthanide energy level scheme by adding a parameter to the model used by Pedrini and experimental input from photoemission spectroscopy (PES)[84–87]. Later, Dorenbos elaborated on the chemical shift in lanthanide physics[48,88]. For a detailed historical survey on the chemical shift and the various effects influencing it, we refer to chapter 5 of[86].

The parameterization of the chemical shift by Thiel and Dorenbos and the equivalence of both approaches are elucidated in appendix A. Despite the simplifying rationale of the model, it can explain some features of lanthanide spectra without cherishing the ambition to serve as a microscopic theory describing the electronic structure of lanthanide compounds, as this requires a framework of quantum mechanical many-body theory. In practice it is recommended to use the model only as a set of empirical rules yielding energy level schemes that are able to describe certain electronic and optical properties.

A linguistic confusion might arise about the term chemical shift. As defined in Eq. 2, the chemical shift is a physical observable which can be calculated in multiple theoretical frameworks. The designation *chemical shift model* as introduced by Dorenbos pertains to the parameterization of $E_{4\mathrm{f}}^{\mathrm{chem}}(\mathrm{Ln}^{Q+}, A)$ in terms of a Coulomb potential (Eq. A3) and is thus one of all possible parameterizations.

The approach to obtain full vacuum referred binding energy (VRBE) and host referred binding energy (HRBE) level schemes is sketched in the following. Furthermore, in every step of the energy level roadmap (Fig. 3), the induced error is assessed in order to obtain a reliable error margin for every quantity calculated in this way. For averaged values, a single standard deviation was used for the error, i.e. 68% of the values lie within the error margin. Similar for fitted trends, prediction limits of 68% were used, containing the accumulated effect of the uncertainty of the fit based on the available data - the confidence limits - and the scatter of the data around the fitted curve.

All steps of the calculation are summarized in Fig. 3, serving as a guide during reading or as a flow scheme when energy level diagrams for lanthanides inside a given host matrix are to be constructed. Additionally, the result of the error analysis is displayed. The figure in the supplementary information shows explicitly how energy level schemes are drawn from the calculated parameters.

The empirical rules discussed in the remainder of this text contain only those relationships that are directly used to construct energy level schemes. Other relationships exist, such as those between the crystal structure of host compounds and the spectroscopic properties of lanthanide dopants[89–92].

4.1 Vacuum referred impurity level, the chemical shift

The 4f-4f Coulomb repulsion energy of europium, $U(\mathrm{Eu}, A)$, takes a prominent place in the empirical models. This parameter represents the difference in 4f bonding energy of the Eu^{3+} and Eu^{2+} ion ¶ :

$$U(\mathrm{Eu}, A) = E_{4\mathrm{f}}(\mathrm{Eu}^{2+}, A) - E_{4\mathrm{f}}(\mathrm{Eu}^{3+}, A). \qquad (3)$$

For europium ions in free space, the Coulomb repulsion energy amounts to $U(\mathrm{Eu}, \mathrm{free}) = 18.05$ eV[88].

Europium is usually selected as lanthanide of reference because it is the divalent lanthanide on which most experimental data can be found. Two reasons can be devised for this. First, it is the lanthanide which can be stabilized in the divalent charge state most easily. Second, the Eu^{2+} ion is the most interesting lanthanide for designing applicable materials due to its highly tunable emission color across the full visible spectrum.

$U(\mathrm{Eu}, A)$ can be acquired from an empirical relationship which relates this parameter with the centroid shift of the Ce^{3+} ion, $\varepsilon_{\mathrm{c}}(\mathrm{Ce}^{3+}, A)$, i.e. the shift of the barycenter of the $5d^1$ manifold upon incorporation (see §5.2) on the lattice site A under study[93,94]:

¶ The notation and definition of this parameter is reminiscent of the Coulomb correlation parameter in the Anderson and Hubbard models for magnetic impurities. In these models, instead of the sevenfold degenerate f orbitals, a non-degenerate level allowing an occupation of zero, one or two electrons is considered, the Coulomb energy being U in the latter case. In the realistic case of an f shell, Coulomb correlation requires a description in terms of Slater-Condon or Racah parameters (see 3). Therefore, the definition of this parameter is only empirical.

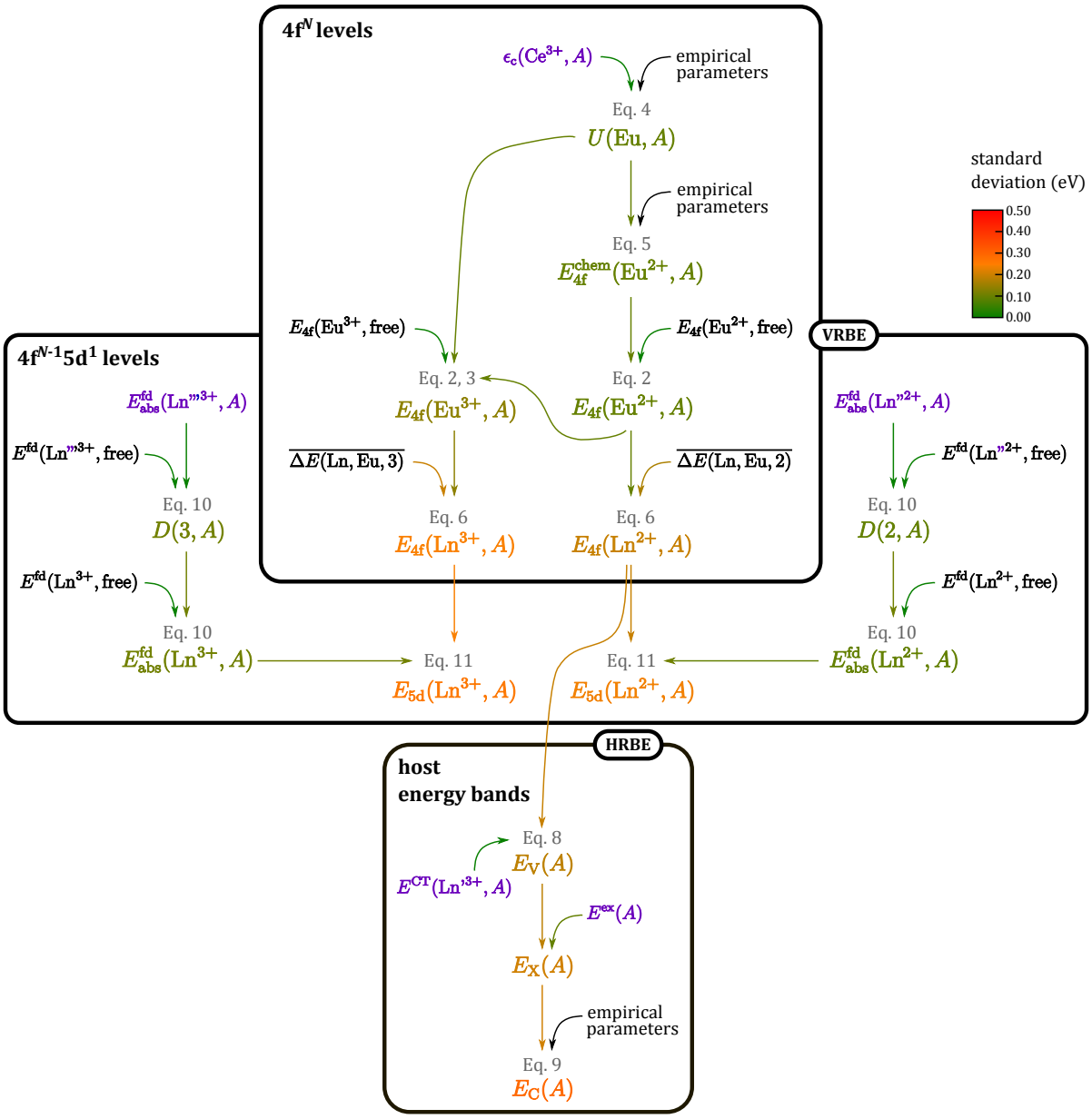

Fig. 3 Lanthanide energy level scheme roadmap. This flow diagram illustrates how VRBE and HRBE level schemes are obtained and which errors are accumulated. Empirical parameters are displayed in black, experimental parameters in purple and the color of calculated quantities maps their standard deviation. Ln′, Ln″ and Ln‴ denote specific lanthanide ions from which input is needed, such as the experimental charge transfer and 4f-5d transition energies (for divalent and trivalent lanthanides).

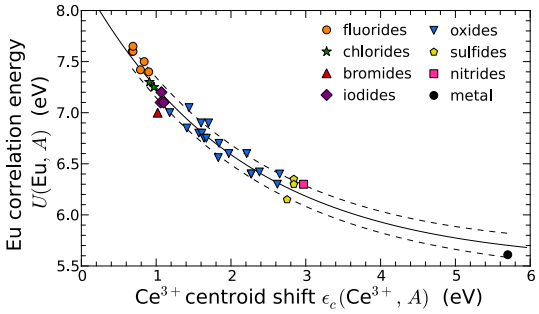

Fig. 4 Experimental Ce^{3+} centroid shifts versus Eu Coulomb correlation energy values for different materials. The solid black line represents the empirical rule, Eq. 4, the dashed lines display the 68% prediction band. Data from [94].

$$U(\mathrm{Eu},A) = 5.44 + 2.834\, e^{-\varepsilon_c(\mathrm{Ce}^{3+},A)/2.2} \quad (4)$$

The obtained value for $U(\mathrm{Eu},A)$ is expected to be less susceptible to random errors compared to the value one could obtain with the aid of a common host referred binding energy level scheme [94]. However, uncertainty originating from the nonlinear least square fitting procedure has to be taken into account.

The 68% prediction limits amount to 100 meV for $U(\mathrm{Eu},A)$ when $\varepsilon_c(\mathrm{Ce}^{3+},A)$ is in the range of 1.0-3.0 eV, which are typical values for Ce^{3+} doped dielectrics. The experimental error on $\varepsilon_c(\mathrm{Ce}^{3+},A)$ is sufficiently small to be ignored as this can directly be obtained from luminescence spectroscopy. The data, fit and associated prediction band, yielding Eq. 4 is displayed in Fig. 4.

One could also calculate $\varepsilon_c(\mathrm{Ce}^{3+},A)$ from crystallographic information of the host compounds, i.e. from the binding distance of the Ce^{3+} ion and its nearest neighbors and electronegativity values of the atomic species contained in the host compound [48,95]. This is not explored in this overview to prevent the introduction of supplementary errors and the relatively straightforward way to obtain $\varepsilon_c(\mathrm{Ce}^{3+},A)$ from experiment (§5.2).

Subsequently, the chemical shift (in eV) of the Eu^{2+} ion is obtained from the empirical formula [48,88]:

$$E_{4f}^{\mathrm{chem}}(\mathrm{Eu}^{2+},A) = \frac{U(\mathrm{Eu},\mathrm{free}) - U(\mathrm{Eu},A)}{0.777 - 0.0353\, U(\mathrm{Eu},A)} \quad (5)$$

The numbers in this formula were chosen to yield reliable chemical shifts for lanthanides in LaF_3, aqueous solution and lanthanide metals [88]. It is therefore rather difficult to estimate the error on $E_{4f}^{\mathrm{chem}}(\mathrm{Eu}^{2+},A)$ as calculated by Eq. 5. If a standard deviation of two units in the last digit of the numbers is taken into account, standard deviations for $E_{4f}^{\mathrm{chem}}(\mathrm{Eu}^{2+},A)$ in the range of 100-110 meV are obtained through propagation. Now $U(\mathrm{Eu},A)$ and $E_{4f}^{\mathrm{chem}}(\mathrm{Eu}^{2+},A)$ are known, the VRBE of the Eu^{2+} and Eu^{3+} ions can be calculated from Eq. 2 and 3 with associated standard deviations of 100 meV and 150 meV respectively. The lowest 4f states can then be added to the energy level scheme (Fig. S1-a,b).

4.2 Shape of the 4f zig-zag curves

Now that the lowest 4f single-particle states of the Eu^{2+} and Eu^{3+} ions are localized with respect to the vacuum level, the zig-zag curves connecting the 4f levels of the different lanthanides can be constructed (Fig. S1-c). Zig-zag refers to the particular shape of this curve emerging from the gradual filling of the 4f shell across the lanthanide series. The 4f electrons are more tightly bound when the shell is completely or half filled, i.e. when 14 or 7 f electrons are present. This is reflected in the ionization energies of the free lanthanide ions [96]. Since the same trend is observed for the $4f^N$-$4f^{N-1}5d^1$ transition energies, the binding energies of the 5d electrons is approximately equal for all lanthanide ions with the same charge state (see §4.5).

The 4f zig-zag curves are defined by the difference in binding energy between the lanthanide ions and the europium ion:

$$\Delta E(\mathrm{Ln},\mathrm{Eu},Q,A) = E_{4f}(\mathrm{Ln}^{Q+},A) - E_{4f}(\mathrm{Eu}^{Q+},A). \quad (6)$$

In the lowest order of approximation, one could assume that the shape of these curves is unchanged when lanthanide ions are brought from the vacuum into the host lattice. This is however a poor approximation as the 4f curves are subject to a rotation (with the Eu ion as pivoting point) attributed to the slightly different crystal field experienced by the different ions due to their unequal ionic radii (see appendix A) [84,85,88]. There are two ways to account for this rotation.

The first possibility, which is most commonly used, is to utilize averaged ΔE parameters, $\overline{\Delta E(\mathrm{Ln},\mathrm{Eu},Q)}$. These were determined by averaging the shape of the zig-zag curves over a large number of host materials and are thus host independent [48].

The second possibility is to calculate a host specific version of ΔE by taking the degree of rotation into account in an empirical way. To acquire this, the contraction tilt parameter $\alpha(Q,A)$ is utilized (see appendix A):

$$\begin{aligned} E_{4f}(\mathrm{Ln}^{Q+},A) = & E_{4f}(\mathrm{Ln}^{Q+},\mathrm{free}) + E_{4f}^{\mathrm{chem}}(\mathrm{Eu}^{Q+},A) \\ & + \alpha(Q,A)\left[R(\mathrm{Ln}^{Q+}) - R(\mathrm{Eu}^{Q+})\right] \end{aligned} \quad (7)$$

It can be calculated from Eq. A9 (see appendix A). In this equation f takes the lattice relaxation around the lanthanide impurity into account, R is the ionic radius [97]. In this work, f is taken to be 0.6 [48]. The real value of f depends however on the elastic properties of the host crystal and can only be assessed by advanced experimental techniques such as X-ray absorption spectroscopy (XAS) or calculation from first principles. Although Eq. A9 has some *theoretical* justification, it is not expected that the chemical shift model can really account for all the details of the interactions between metal ions and their crystalline environment. If correct values are used for the quantities in the right hand side of Eq. A9, one can calculate $\Delta E(\mathrm{Ln},\mathrm{Eu},Q,A)$

values which are as close to $\overline{\Delta E(\mathrm{Ln},\mathrm{Eu},Q)}$ as 50-150 meV. In any case, the similar values for $E_{4f}^{\mathrm{chem}}(\mathrm{Eu}^{Q+},A)$ regardless of A indicate that only small variations in $\alpha(Q,A)$ are expected and the $\overline{\Delta E(\mathrm{Ln},\mathrm{Eu},Q)}$ values should be sufficiently accurate.

For the Ln^{2+} ions, the average $\overline{\Delta E(\mathrm{Ln},\mathrm{Eu},2)}$ values were determined by Dorenbos from Ln^{3+} charge transfer (CT) energies ($E^{\mathrm{CT}}(\mathrm{Ln}^{3+},A)$, see §4.3 and §5.4). For Sm^{3+}, Tm^{3+} and Yb^{3+}, a sufficient amount of data was available to reliably pin the $\overline{\Delta E(\mathrm{Ln},\mathrm{Eu},2)}$ values within a standard deviation of typically 150 meV[98,99]. For Pr^{3+}, Nd^{3+}, Dy^{3+}, $Ho^{3+}$and Er^{3+} only a few or even one CT data point was available to calculate the average[98]. For these ions, we estimate a standard deviation of 200 meV.

For the Ln^{3+} ions, initially, the rule of thumb $\overline{\Delta E(\mathrm{Ln},\mathrm{Ce},3)} = 1.2\ \overline{\Delta E(\mathrm{Ln},\mathrm{Ce},2)}$ was used together with the known values of $\Delta E(\mathrm{Ln},\mathrm{Eu},Q,\mathrm{free})$ for the shape of the free Ln^{3+} ions 4f curve[98]. A first improvement of this model was introduced by estimating binding energies of Ln^{3+} by pinning thermally quenched 5d levels close to or in the conduction band[98] . Recently, more accurate parameters were obtained from the intervalence charge transfer (IVCT) energies of Pr^{3+} and Tb^{3+} in transition metal containing compounds (see §5.4)[92,100]. Since these transitions were only investigated for these two ions, more uncertainty is presumed for the shape of the Ln^{3+} 4f curve. In analogy with the Ln^{2+} 4f curve, a standard deviation of 200 meV is adapted.

When the standard deviation for $E_{4f}^{\mathrm{chem}}(\mathrm{Eu}^{Q+},A)$ is propagated through Eq. A9, standard deviations of 1-2 meV/pm are obtained for $\alpha(Q,A)$, yielding standard deviations of 150 meV for $\Delta E(\mathrm{Ln},\mathrm{Eu},Q,A)$.

Hence, using the average shape of the zig-zag curves ($\overline{\Delta E(\mathrm{Ln},\mathrm{Eu},Q)}$) or a host compound specific one ($\Delta E(\mathrm{Ln},\mathrm{Eu},Q,A)$ through calculation of $\alpha(Q,A)$) gives rise to a similar accuracy.

4.3 Fixing the valence band

Now the vacuum referred binding energies (VRBE) of the lowest 4f levels are determined. They should be positioned with respect to the energy bands of the host compound (HRBE). Charge transfer (CT) energies of trivalent lanthanides are used to probe the distance between the top of the host's valence band (VB) and the lowest 4f ground state of the associated divalent lanthanide[98]. In this way, the valence band of the host is added to the energy level scheme (Fig. S1-d).

The thermodynamic charge-state transfer energy was used to define the *impurity levels* of the lanthanide ions. As explained in §3, optical absorption experiments yield an energy value which is larger than the thermodynamic one due to a relaxation of the nuclear positions. Within this empirical framework, the distinction between the thermodynamic and optical charge-state transition energies is neglected, giving rise to intrinsic errors. Furthermore, the breakdown of Koopmans' theorem due to covalent renormalization and correlation effects prevents to consider a charge transfer transition in terms of single-particle orbitals, i.e. the energy of the transition is determined from Eq. 1.

Since errors were already taken into account for the shape of the 4f curves, no additional error is induced in pinning the valence band with respect to the 4f curves. The experimental error on the charge transfer energy depends on the exact features of the spectrum (see §5.4). For current error assessment, the best case scenario, corresponding with an experimental error of 10 meV is adapted since the accuracy of the empirical models is the main topic of this work.

The vacuum referred binding energy of valence band electrons, i.e. the photoelectric threshold, $E_{PE}(A)$, is calculated as:

$$E_{\mathrm{V}}(A) = -E_{PE}(A) = E_{4f}(\mathrm{Eu}^{2+},\mathrm{free}) + E_{4f}^{\mathrm{chem}}(\mathrm{Eu}^{2+},A) + \overline{\Delta E(\mathrm{Ln},\mathrm{Eu},2)} - E^{\mathrm{CT}}(\mathrm{Ln}^{3+},A) \quad (8)$$

The uncertainty on $E_{PE}(A)$ is obtained from the uncertainties on all terms in Eq. 8, yielding standard deviations in the range of 150-200 meV. The most reliable value for $E_{PE}(A)$ is thus obtained if the CT energy of the Eu^{3+} is used, as in this case the third term in Eq. 8 vanishes (Ln = Eu). This quantity is experimentally accessible through X-ray or Ultraviolet Photoelectron Spectroscopy (XPS or UPS)[101]. Since these are surface techniques, the experimental value of E_{PE} is highly dependent on which surface of the crystal is probed and on possible surface reconstruction and passivation[101]. In the case of metals, the work function - defined as the energy difference between the vacuum level and the chemical potential of the electrons - is identical to the photoelectric threshold[101]. It is sometimes overlooked that this is not true in the case of insulators or semiconductors where the chemical potential lies inside the forbidden band[101].

4.4 Self-trapped excitons and the conduction band

The conduction band (CB) can be added to the energy level scheme if the electronic band gap energy ($E_G(A)$) is known. This can be obtained by adding the exciton binding energy ($E_{e-h}^{ex}(A)$) to the optical band gap ($E^{ex}(A)$) as displayed in Fig. S1-e,f.

The optical band gap value is typically determined from absorption spectroscopy or diffuse reflection spectroscopy on powders, combined with Kubelka-Munk (KM) fitting of the absorption coefficient (see §5.5). The rather inaccurate nature of this technique in the case of powder reflection spectroscopy does not allow to neglect the error on this experimental parameter. One standard deviation is estimated to be 100 meV (§5.5).

To obtain the electronic band gap, one needs the excitonic binding energy in addition. Unfortunately, this quantity is hard to determine. To meet this difficulty, a rule of thumb was introduced in[102] to relate the electronic and optical band gap values:

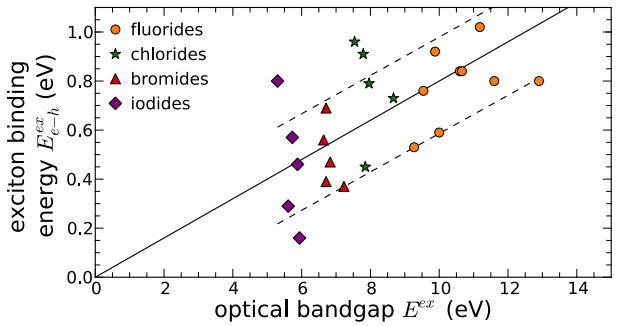

Fig. 5 Experimental exciton binding energies versus optical band gap values for halide wide band gap semiconductors. The solid black line represents the $E^{ex}_{e-h}(A) = 0.08E^{ex}(A)$ rule, the dashed lines display the 68% prediction interval for the linear fit. Data from [103].

$$E_G(A) = 1.08E^{ex}(A) \tag{9}$$

The 1.08 proportionality factor was determined as the average of the limited available data.

The error on the location of the conduction band depends on the accuracy of the *1.08-rule of thumb*. In Fig. 5, the underlying data to obtain this rule are displayed. The proportionality between the optical band gap energy and the exciton binding energy of a compound is not so clear. However, thanks to the small binding energies of (self-trapped) excitons compared to the band gap of the considered material classes, the large relative error for $E^{ex}_{e-h}(A)$ (in the order of 20-100%) reduces to a moderate relative error for $E_G(A)$, corresponding with a standard deviation of typically 250 meV if both the experimental uncertainty on $E^{ex}(A)$ and the limited accuracy of Eq. 9 are taken into account.

If needed, the electron affinity, $\chi(A) = -E_C(A)$, can be obtained by subtracting $E_G(A)$ from $E_{PE}(A)$, yielding standard deviations in the range of 250-350 meV [101]. With this kind of modeling, the electron affinity of a semiconductor or dielectric can easily be obtained from lanthanide spectroscopy [93,94,101,104].

The valence stability of the divalent ions in a particular host can be estimated from the location of the lowest Ln^{2+} 4f level with respect to the host's energy bands. This is true by definition of the charge-state transition levels (see §3). Dorenbos confirmed the validity of the empirically found 4f levels as charge-state transition levels for multiple compounds [105]. The location of the electronic chemical potential is assumed to be halfway the band gap. This is only formally true at absolute zero and in the case when the effective masses of electrons and holes are equal [106]. Furthermore, the location of the chemical potential is supposed to be unaltered upon introduction of the dopants. The energy difference between the center of the band gap and the relevant Ln^{2+} $4f^N$ level can be calculated with a standard deviation of 250 meV for Eu^{2+} and 300 meV for Sm^{2+}, Tm^{2+} and Yb^{2+}. Of course, the occurrence of defects can shift the chemical potential away from the center of the band gap. These defects can be intrinsically present, be a consequence of charge compensation schemes or induced via co-doping or treatment in specific gas atmospheres [105]. The specific shape of the 4f zig-zag curve which is to a large extent host-compound independent explains why Eu^{2+} is the most abundant divalent lanthanide, followed by Yb^{2+}, Sm^{2+} and Tm^{2+}.

4.5 Interconfigurational 4f-5d transitions

In lanthanide spectroscopy, $4f^{N-1}5d^1$ configurations play often a crucial role. Therefore, the multiplets, corresponding with this configuration need to be added to the total energy level scheme. Formally, this does not pose any new difficulties and the idea of the pseudo-ion remains valid. The $4f^N$ multiplets can be generalized to $4f^{N-1}5d^1$ multiplets, provided a suitable coupling scheme.

Also, in the case of the empirical energy level schemes that are reviewed in this paper, adding the 5d level does not pose any additional difficulty. The significance of this level as a charge-state transition energy is clear. When the chemical potential as well as the thermodynamic 4f charge-state transition level are higher than the 5d level, a $4f^{N-1}5d^1$ ground state is to be expected rather than a $4f^N$ ground state. This can be the case for certain divalent lanthanides [107,108].

Typically, it is assumed that the spectroscopic redshifts ($D(Ln^{Q+},A)$), i.e. the decrease in $4f^N$-$4f^{N-1}5d^1$ absorption energy between the free and incorporated ion,

$$D(Ln^{Q+},A) = E^{fd}(Ln^{Q+},\text{free}) - E^{fd}_{abs}(Ln^{Q+},A), \tag{10}$$

are equal for all lanthanide ions having the same charge, regardless of their differing ionic radii [48]. The spectroscopic redshift was first introduced by Dorenbos in his large-scale investigation of reported transition energies [109]. However, the idea that the $4f^N$-$4f^{N-1}5d^1$ transition energies of the lanthanide ions are related is much older [110–112].

The energy of the $4f^N$-$4f^{N-1}5d^1$ transition was first investigated in great detail for the trivalent ions, mainly based on data for Ce^{3+}, Pr^{3+} and Tb^{3+}, confirming the known trend within a standard deviation of 100-115 meV. More data, underpinning this rule, was gathered during the last 20 years.

For the divalent lanthanides, similar data mining was performed, mainly based on electronic spectra of the Eu^{2+}, Yb^{2+} and Sm^{2+} ions [113]. The associated standard deviations amount to 50-100 meV. Other divalent lanthanides are very difficult or impossible to stabilize in compounds (see §4.4) leading to a lack of available data for the redshifts.

These standard deviations pertain to the $4f^N$-$4f^{N-1}5d^1$ absorption energies. For the VRBE of the 5d level, the uncertainty on the location of the 4f level has to be added

$$E_{5d}(Ln^{Q+},A) = E_{4f}(Eu^{Q+},\text{free}) + E_{4f}^{chem}(Eu^{Q+},A) + \overline{\Delta E(Ln,Eu,Q)} + E^{fd}(Ln^{Q+},\text{free}) - D(Q,A), \quad (11)$$

leading to standard deviations of 250-300 meV. If the location of the 5d level with respect to the host's valence band is required, one obtains:

$$E_{5d}(Ln^{Q+},A) - E_V(A) = E^{fd}(Ln^{Q+},\text{free}) - D(Q,A) - \delta_{Q,3}U(Eu,A) + \overline{\Delta E(Ln,Eu,Q)} - \overline{\Delta E(Ln',Eu,2)} + E^{CT}(Ln'^{3+},A), \quad (12)$$

where Ln'^{3+} is the lanthanide ion for which the CT energy was used to pin the valence band. For the Kronecker delta, $\delta_{Q_1,Q_2} = 1$ if $Q_1 = Q_2$ and $\delta_{Q_1,Q_2} = 0$ if $Q_1 \neq Q_2$. If Ln = Ln' and $Q = 2$, this relationship simplifies to the often used formula:

$$E_{5d}(Ln^{2+},A) - E_V(A) = E_{abs}^{fd}(Ln^{2+},A) + E^{CT}(Ln^{3+},A). \quad (13)$$

In this case, the uncertainty is the experimental accuracy for probing both parameters on the right hand side of Eq. 13. In the more general case, a higher uncertainty is obtained, coming from the $\overline{\Delta E}$ terms. If the energy difference between the 5d level and the exciton binding energy or the CB bottom is needed, additional contributions to the standard deviation have to be considered.

In 2003, a linear relationship was proposed between the redshifts of the divalent and trivalent lanthanide ions, based on data from Ce^{3+} and Eu^{2+} spectra:

$$D(Eu^{2+},A) = 0.64D(Ce^{3+},A) - 0.233 \text{ eV}. \quad (14)$$

The data underlying this empirical rule is shown in Fig. 6, where error margins are given, corresponding with the 68% prediction interval, amounting to 250 meV.

By spectroscopic measurement of one $4f^N$-$4f^{N-1}5d^1$ energy for each valence state (or for one valence state, supplemented with formula 14), one can add the locations of the $4f^{N-1}5d^1$ states for all ions to the energy level scheme (Fig S1-g,h).

4.6 Vibronic interactions

Up to now only static interactions between the luminescent ion and the host crystal have been considered. No attention has been paid to vibronic interactions resulting from the coupling of electronic states and vibrational modes of the defect cluster. However, this interaction has a strong influence on the spectroscopic properties of the compound. Vibronic broadening of emission and excitation bands and the Stokes shift are direct consequences of this interaction.

The Stokes shift, ΔS, is defined as the energy difference between the absorbed and emitted photons originating from transitions between the lowest ground state (in this case the lowest $4f^N$ multiplet) and excited state (in this case the lowest $4f^{N-1}5d^1$ multiplet):

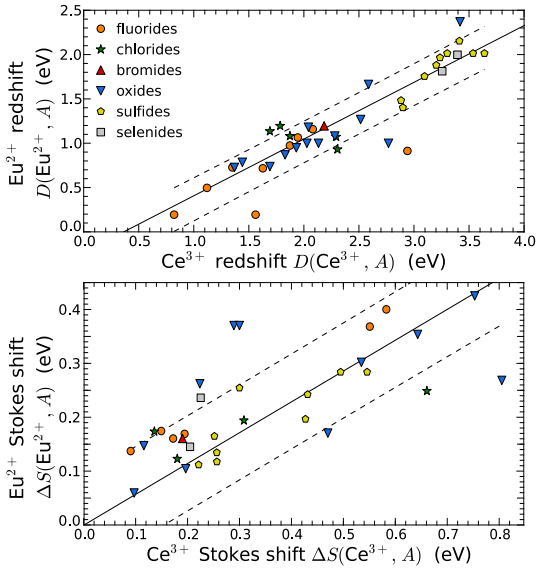

Fig. 6 Top: Spectroscopic redshifts of Ce^{3+} versus those of Eu^{2+} on the same lattice site. The solid black line represents the empirical rule, given by Eq. 14. The dashed lines display the 68% prediction interval for the linear fit. Bottom: Similar figure for the Stokes shifts and the empirical rule given by Eq. 16. Data from [114,115].

$$\Delta S(Ln^{Q+},A) = E_{abs}^{fd}(Ln^{Q+},A) - E_{em}^{fd}(Ln^{Q+},A), \quad (15)$$

Similar to the redshift, it has been proposed that the Stokes shifts of Ln^{Q+} $4f^N$-$4f^{N-1}5d^1$ transitions are the same for all ions with the same charge in the same host crystal [109,113,115]. This was first substantiated for trivalent lanthanides, based on data from UV and VUV spectroscopy of Ce^{3+}, Pr^{3+}, Nd^{3+}, Er^{3+} and Tm^{3+} ions. The trend holds within a standard deviation of 15 meV. For divalent lanthanides, a similar trend has been shown for Sm^{2+}, Eu^{2+}, Tm^{2+} and Yb^{2+} within a standard deviation of 30 meV.

Stokes shifts for the $4f^N$-$4f^{N-1}5d^1$ intraconfigurational transitions of the Eu^{2+} and Ce^{3+} ions were compared in [116]. A positive correlation is clearly present and the values were connected through a linear fit,

$$\Delta S(Eu^{2+},A) = 0.61\Delta S(Ce^{3+},A). \quad (16)$$

This fit is displayed in Fig. 6. Prediction intervals are situated at about 100 meV above and below the fitted value for $\Delta S(Eu^{2+},A)$, corresponding to relative errors in the range of 20-80%. If the energy of Eu^{2+} emission in a certain host is to be estimated from spectroscopy of the Ce^{3+} ion, one needs to apply Eq. 14 and Eq. 16 consecutively yielding standard deviations of 270 meV. For example, if the lowest energy 4f-5d absorption band of Ce^{3+} is situated at 400 nm and shows a Stokes shift of 0.25 eV, the emission of the Eu^{2+} ion in the same host is predicted at 525 nm using Eq. 10, 14, 15 and 16. However, the uncertainty

interval corresponding with a single standard deviation of 270 meV ranges from 470 nm to 595 nm, spanning a significant fraction of the visible spectrum, ranging from blue to orange light emission. For this reason, these kinds of relationships have limited use for designing LED phosphors where specifications for emission peak wavelengths have a typical tolerance of a few to 10 nm.

Furthermore, the width of the emission band cannot be assessed from these empirical relations while this is of major importance for the emission color of the phosphor. This can deviate strongly from host to host for the same luminescent ion, for example $Ba_{0.8}Sr_{0.2}SiO_4:Eu^{2+}$ shows an emission band full width at half maximum (FWHM) of 84 nm while for $SrGa_2S_4:Eu^{2+}$, the FWHM is only 52 nm. Emission bands of both materials are nevertheless located in the same wavelength range[117,118]. Within a configuration coordinate model (see further), the emission band width can be expressed in terms of the Stokes shift and a phonon frequency, related to the host[119]. Dorenbos applied this on a large number of Eu^{2+} activated crystals[114]. This model is however not sufficiently accurate to be used for practical applications[114].

The effects of vibronic interactions are hence not very well described by the empirical models. An important remark regarding the empirical energy level schemes is that all excited states (including CT transitions to fix the position of the top of the valence band) were derived from excitation spectra (or alternatively absorption spectra). Though this is the most straightforward way to assess the excited state landscape, one should not forget that in this way one does not consider the excited state in its relaxed form, i.e. the lowest vibrational energy level. This is illustrated in Fig. 7. Herein, a one-dimensional cross section of the multidimensional potential energy (or Born-Oppenheimer) surfaces is shown within the harmonic approximation, simplifying the real situation because of the high dimensionality of nuclear coordinate space, anharmonic effects, unequal vibronic coupling in ground and excited states and interactions or crossovers between the multiple potential energy surfaces. Nevertheless, phenomenological interpretation is often possible thanks to this simplified so-called configuration coordinate diagram.

During excitation, a vertical transition occurs, corresponding to the energy of the absorbed photon. This is the energy which is used for constructing the energy level schemes. However, almost immediately after the photon absorption, a relaxation of the excited state occurs towards the lowest vibrational state of the excited state potential energy surface (at absolute zero temperature). It would be more appropriate to display this energy (i.e. the energy of the zero phonon line, ZPL) in purely electronic energy level schemes. Zych and coworkers have succeeded in obtaining more accurate $\overline{\Delta E(\mathrm{Ln},\mathrm{Ce},3)}$ values from measurement of the ZPL of Ln^{3+} $4f^N$-$4f^{N-1}5d^1$ transitions in four different host's[120]. The applicability of this approach is however limited since ZPLs are most often obscured in spectra

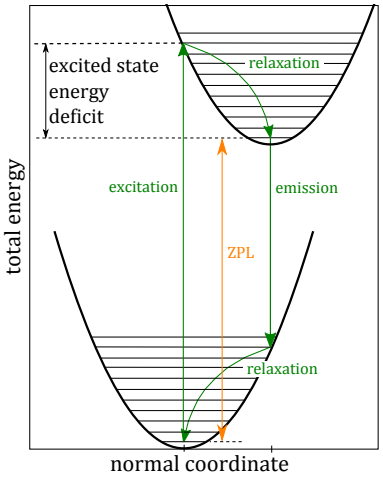

Fig. 7 Configuration coordinate diagram representing a system with two electronic levels, featuring the same single vibrational mode. Vibronic interactions can often be rationalized within a simple model as the displayed one.

of 4f-5d transitions. Additionally, in designing materials for a specific application, the emission band maximum and FWHM are more important parameters than the location of the ZPL, both requiring a more detailed knowledge of the specific nature of vibronic interactions.

4.7 Thermal quenching of luminescence

Luminescent materials show a particular response as a function of temperature. Most often, the photoluminescence quantum efficiency - i.e. the ratio of the number of emitted to the number absorbed photons[2,121] - drops when temperature rises above a certain critical temperature. Observationally, an energy barrier, ΔE_T, can be associated with thermal quenching. Then, the thermal quenching (TQ) profile of the material is described by:

$$I(T) = I(0)\left(1 + \frac{\tau_v}{\tau_0} e^{-\Delta E_T / k_B T}\right)^{-1} \quad (17)$$

where τ_v is the intrinsic radiative decay constant of the ion and τ_0 is the decay constant for the non-radiative decay path, responsible for TQ.

According to Blasse, this empirically determined energy barrier corresponds to the energy difference between the emitting excited state and the conduction band of the host material in the case of the $4f^1$-$5d^1$ transition of Ce^{3+}[122]. This idea was extended to other $4f^N$-$4f^{N-1}5d^1$ transitions by multiple authors through the comparison of energy level schemes and TQ experiments[123–126]. Within this theoretical framework, one can calculate the TQ behavior from the constructed energy level scheme. It is however not very clear whether the CB bottom, the lowest exciton level or some intermediate value has to be used. Note that in transition metal host compounds, TQ can proceed via an IVCT state (see §5.4).

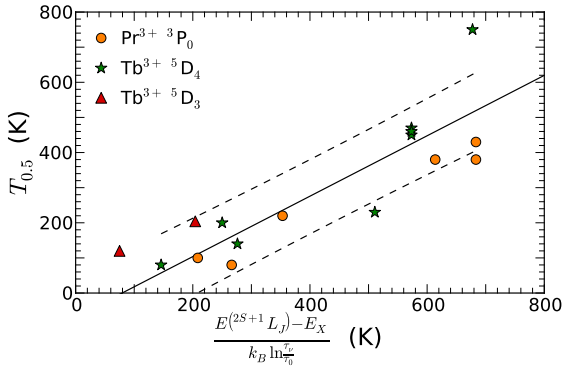

Fig. 8 Experimental versus calculated $T_{0.5}$ for Pr^{3+} $^3P_0$ emission and Tb^{3+} $^5D_4$ and $^5D_3$ emission. E_X represents the VRBE of a self-trapped exciton, $E(^{2S+1}L_J)$ of the emitting $4f^N$ level. τ_v was taken to be 1 ms, 0.5 ms and 0.1 ms for $^5D_4$, $^5D_3$ and $^3P_0$ emission, respectively. A straight line is fit (slope 0.86, intercept -68 K) and the 68% prediction interval is shown. Data from [129]. Points where only an upper or lower border was given, were omitted.

Moreover, reliable values for the parameters τ_v and τ_0 in Eq. 17 are needed. The lifetime of the excited state can be obtained from time-resolved luminescence spectroscopy. It is in general not sufficient to utilize a predetermined value for τ_v as the radiative decay probability of an ion is sensitive to the embedding host [127,128]. τ_0 has the meaning of a frequency factor or attempt rate. The period of the main vibrational mode at the defect site is taken for τ_0 which is around $0.5-1 \times 10^{-13}$ s [126,129].

ΔE_T can be obtained from TQ measurements using two methods: one can fit Eq. 17 to the experimental quenching profile, or one can take $T_{0.5}$, i.e. the temperature where the intensity reaches 50% of the intensity at low temperature, as sole experimental parameter. This is then related to ΔE_T by:

$$T_{0.5} = \frac{\Delta E_T}{k_B \ln \frac{\tau_v}{\tau_0}} \tag{18}$$

as obtained from Eq. 17. Recently, Dorenbos and Rogers studied the Tb^{3+} $^5D_4$ and $^5D_3$ emissions and the Pr^{3+} $^3P_0$ emission in more detail for transition metal oxide host compounds, allowing a determination of the accuracy of this method [129]. In this work, the thermal quenching of the interconfigurational 4f transitions is ascribed to the presence of a IVCT state. The available data is displayed in Fig. 8.

Though one would expect a unit slope straight line through the origin, the fitted line intersects the horizontal axis around 70 K. This is attributed to the exact geometry of the potential energy surfaces (approximated as 1D parabola) in nuclear coordinate space in [129]. Since our interest is oriented towards the deviations from the trend line, neither the nonzero intercept nor the exact nature of the thermal quenching are of interest at this moment.

From the 68% prediction intervals, displayed in Fig. 8, the accuracy in determining $T_{0.5}$ from an energy level scheme is limited to 115 K for the Tb^{3+} and Pr^{3+} ions. A substantial fraction of the inaccuracy is coming from the ΔE_T value. If one uses the self-trapped exciton lowest energy level as "end point" for the thermal quenching process, ΔE_T is obtained from

$$\begin{aligned}\Delta E_T(\mathrm{Ln}^{Q+},A) &= E_X(A) - E_{\text{emitting level}}(\mathrm{Ln}^{Q+},A) \\ &= E^{ex}(A) - E^{\mathrm{CT}}(\mathrm{Ln}'^{3+},A) - E^{\text{transition}}_{\text{abs}}(\mathrm{Ln}^{Q+},A) \\ &\quad + \delta_{Q,3}U(\mathrm{Eu},A) + \overline{\Delta E(\mathrm{Ln}',\mathrm{Eu},2)} - \overline{\Delta E(\mathrm{Ln},\mathrm{Eu},Q)},\end{aligned} \tag{19}$$

inducing standard deviations in the range of 300-350 meV. If these standard deviations are propagated through Eq. 18, standard deviations for $T_{0.5}$ in the range of 160 K, 220 K and 280 K are obtained for Tb^{3+} $4f^8(^5D_4)$, Eu^{2+} $4f^6 5d^1$ and Ce^{3+} $5d^1$ emission respectively. These values are obtained without taking any additional error for τ_v and τ_0 into account. It is seen that, while trends are usually able to predict transition energies and absolute level positions with sufficient accuracy, this type of model fails for the determination of TQ, since the standard deviations on the quenching temperature become excessive.

In the common reasoning which was sketched above, the calculation of the energy barrier height uses the location of the excited state as obtained from absorption or excitation spectroscopy. Again, the role of geometrical relaxation after photon absorption is not included. Thermal ionization of the defect is governed through the thermodynamic charge-state transition level, rather than the optical counterpart which was used to construct the energy level scheme. Nonetheless, the error margins are too large for accurate prediction of the thermal quenching temperature $T_{0.5}$.

Moreover, in reality, multiple competing (non-radiative) decay mechanisms exist, all having a different temperature response or nonequivalent luminescent centra might exist. For these reasons, thermal quenching (and decay dynamics) are very complex phenomena for which a simple model as Eq. 17 is inappropriate to grasp the details.

The reason for the large error margins on the calculated $T_{0.5}$ value originates from the uncertain determination of the location of the conduction band bottom due to the combined effect of the inaccurate determination of $E^{ex}(A)$ and the large error on Eq. 9.

In summary, a correct description of thermal ionization requires more details of the energy landscape which are harder to obtain from spectroscopic experiments.

Thermal quenching is not the only phenomenon for which conduction band states are thought to be involved. Anomalous luminescence, i.e. the light emission coming from the decay of an excited state containing an impurity trapped exciton - which is a different excitation than a self-trapped exciton - and electron transfer, possibly leading to charge storage and delayed luminescence

are typical examples[23,130–133]. Due to above mentioned reasons, quantitative predictions of these phenomena are not straightforward and in reality, empirical energy level schemes need to be considered as a qualitative aid in understanding experimental results rather than a way to predict experimental results[134,135]. First principles calculations can additionally be of great help to understand individual cases[136,137].

5 Spectroscopic guidelines

The previous section intended to show the route and obstacles along the energy level roadmap and point out the induced errors along the way. The experimental determination and accuracy of the input parameters was not mentioned in detail. To complete the picture, a more thorough look is cast on the experimental aspects for the determination of the input parameters.

5.1 Wavelength and energy units

For the purpose of energy level modeling, optical spectra are interpreted on a physically more sound energy scale than on wavelength scale which is often the output from experiments. Depending on which type of measurement is performed, a different treatment is needed to convert spectra from wavelength to energy units. The equidistant wavelength intervals in which emission spectra are measured are not equidistant on energy scale due to the inverse proportionality between wavelength and photon energy. For this reason, the ordinates of the data points of emission scans, measured in equidistant wavelength intervals, have to be multiplied with $\frac{hc}{E^2}$ to obtain the correct spectrum on energy scale[138]. Absorption and excitation scans on the other hand do not require this conversion because these spectra are measured in a relative fashion with respect to the spectrum of the light source used during the measurement[139].

5.2 Ce^{3+} Centroid shift

The $4f^N$-$4f^{N-1}5d^1$ excited states are effectively probed by photoluminescence (PL) excitation spectroscopy. Especially the simple electron configuration of the Ce^{3+} ion allows for straightforward interpretation of its $5d^1$ excited state and calculation of the centroid shift of the considered lattice site A, $\varepsilon_c(Ce^{3+},A)$, defined as the energy difference of the barycenter of the $5d^1$ manifold in free space and on the lattice site:

$$\begin{aligned}\varepsilon_c(Ce^{3+},A) &= \frac{1}{10}\left[6E^{fd_{5/2}}(Ce^{3+},\text{free}) + 4E^{fd_{3/2}}(Ce^{3+},\text{free})\right] \\ &\quad - \frac{1}{5}\sum_{i=1}^{5} E_{abs}^{fd_i}(Ce^{3+},A) \\ &= 6.35\ \text{eV} - \frac{1}{5}\sum_{i=1}^{5} E_{abs}^{fd_i}(Ce^{3+},A) \qquad (20)\end{aligned}$$

The numerical data for the free Ce^{3+} ion was taken from[140] and $E_{abs}^{fd_i}(Ce^{3+},A)$ $(i = 1..5)$ are the maxima of the excitation bands. These can be experimentally determined with an accuracy of 20 meV provided the bandgap of the host compound is sufficiently large. Since the numerical parameter 6.35 eV was readily included in the derivation of empirical rule Eq. 4, no additional error is taken into account for this parameter with regard to the construction of energy level schemes. The Ce^{3+} $5d^1$ state is split in maximally five components by a crystal field. For high symmetry fields, an incomplete splitting occurs and correct weighing factors have to be associated with the different bands. Knowledge of the symmetry of the defect cluster and a simple parametrization of the crystal field such as a point charge model allows to obtain the degeneracies. This is well documented in the literature on crystal field theory[141].

5.3 $4f^N$-$4f^{N-1}5d^1$ transition energy

Interpretation of the $4f^N$-$4f^{N-1}5d^1$ excitation spectrum is straightforward in the case of Ce^{3+} thanks to the single-electron picture. Unfortunately, this is not the case for the other lanthanide ions for which exact determination of the energy levels is often nontrivial due to the high density of electronic states and vibronic broadening. Nevertheless, to construct a complete energy level scheme, the $4f^N$-$4f^{N-1}5d^1$ absorption energy of at least one divalent lanthanide ion is needed in addition, unless one uses Eq. 14. Therefore some prior knowledge of the electronic structure of the ion under consideration is needed to experimentally extract the lowest energy level of the $4f^{N-1}5d^1$ manifold.

Next to the single 5d electron, mainly subject to the crystal field interaction, an unfilled 4f shell is present in the excited lanthanide ion. In this case, both the 4f crystal field interaction and the 4f-5d Coulomb interaction are assumed to be dominated by the inter-4f Coulomb and 4f spin-orbit interactions. This type of electron configurations are often modeled as a superposition of the single-particle crystal field splitting of the 5d electron and the multiplet structure of the $4f^{N-1}$ configuration of the Ln^{Q+1} ion, i.e. the so-called decoupled perturbation scheme. In this scheme, one assumes implicitly that the interactions between the $4f^{N-1}$ core and the 5d electron, of which the isotropic exchange part of the Coulomb interaction is largest, can be neglected.

The most typical example is the $4f^6 5d^1$ excited state of the Eu^{2+} ion where the $4f^6$ core is modeled by the ^7F_J multiplets of the Eu^{3+} ion. This picture was first described by Freiser, Methfess and Holtzber in 1968[142]. The validity of this approach is often justified by the occurrence of a so-called staircase structure that can be resolved in certain low temperature Eu^{2+} spectra[143–146]. The occurrence of a staircase structure does not necessarily mean that the Coulombic exchange can be neglected and decoupled energy level labels are correct[147–150].

As input for the energy level scheme construction, one needs the location of the lowest level of the $4f^{N-1}5d^1$ manifold for at least one lanthanide. In[114], the location of this level is approximately determined for $N = 7$ from the point where the low en-

ergy side of the Eu^{2+} excitation spectrum reaches 15-20% of the first staircase maximum. Even when Coulombic 4f-5d exchange becomes more important and the decoupled perturbation scheme fails, this approach remains approximately valid to locate the lowest energy $4f^6 5d^1$ state. The less accurate nature of this approach is reflected in an experimental standard deviation of 100 meV.

5.4 Charge transfer band

Charge transfer (CT) energies are important parameters if a host referred energy level scheme is constructed. These excited states, originating from an electron which is transferred from or to a lanthanide ion, yield intense excitation bands in the UV region. An electron transfer from an anion neighbor towards the lanthanide ion is the most common type of charge transfer. This typically concerns trivalent lanthanide ions, yielding a temporary divalent lanthanide until the electron is transferred again to the anion. If the electronic states forming the top of the valence band can be attributed to the neighboring anions, the CT energy indeed probes the distance between the VB top and lowest Ln^{2+} 4f state. This idea already dates back to Jørgensen in the 1960's where a transition between the highest occupied molecular orbital (HOMO) and the Ln 4f shell was identified with the broad absorption bands of molecular lanthanide complexes.[110]. No specific name is in circulation for this kind of CT.

In the second type of CT, the so-called intervalence charge transfer (IVCT), an electron is transferred from the lanthanide ion towards another metal ion inside the host crystal. For this reason, IVCTs are specifically found in transition metal containing hosts. If the acceptor metal can be associated with the electronic states constituting the bottom of the conduction band, IVCTs probe the distance between the lowest 4f state of the lanthanide and the CB bottom. In this case, the electronic configuration of the IVCT state, i.e. a hole in the 4f shell of the lanthanide and an electron in the conduction band of the host, is very similar to the so-called impurity trapped exciton (ITE).

The maximum of the excitation band, corresponding with the charge transfer, is usually chosen as input for the energy level scheme. Frequently, this energy can be simply read from the spectrum with a small experimental error. It is however not uncommon that multiple CT transitions are present in the spectrum, possibly obscured by $4f^N$-$4f^{N-1}5d^1$ or $4f^N$-$4f^N$ absorption bands. In this case, resolving the desired energy value can be more challenging and a larger experimental error is expected.

5.5 Optical band gap

As the optical band gap is a quantity solely related to the host, it is recommended that undoped host materials are used to obtain the band gap rather than doped samples where absorption bands of the dopant can obscure the measurement. The optical band gap can be measured by transmission spectroscopy in the case of single crystals, thin films or glasses and by diffuse reflectance spectroscopy in the case of powder samples. In the former case, the Lambert-Beer equation can be used to obtain an absorption spectrum, in the latter case the Kubelka-Munk model is the most straightforward way to obtain an absorption spectrum from the measured reflection spectrum[151]. When an absorption spectrum is available, the band gap can be estimated by fitting of the absorption coefficient. The exact expression to be used for the fitting depends on the type of band gap (direct or indirect) and the nature of the electronic transition (allowed or forbidden) which are often unknown. Ideally, the type of band gap can be determined from choosing the best fit among the different possible equations, but this requires a very good experimental data set, which is seldom obtained. Of course, this could be determined from electronic band structure calculations, though the necessary computational effort would nullify the biggest asset of the employed empirical models, its simplicity and fast implementation.

Given the approximate character of both the Kubelka-Munk procedure as the fitting of the absorption spectrum, a standard deviation of at least 100 meV has to be considered when the optical band gap of powders is assessed from diffuse reflectance spectroscopy.

5.6 Multiple lattice sites and impurity phases

In the above treatment it was only briefly mentioned that the notation *A* denotes the lattice site on which the lanthanide ion incorporates rather than the host material under study. If only one lattice site is occupied by the lanthanide ion both meanings are equivalent. More complicated cases are however common[152–158]. If two nonequivalent lattice sites are available for the lanthanide ions, the different local structure will give rise to different luminescence behavior for the same ion on each site. In this case, a correct description of the electronic structure of the lanthanide doped material requires a separate energy level scheme per different nonequivalent site.

When the different lanthanide ions do not show the same behavior with respect to incorporation on different lattice sites of a specific host compound, additional complications arise. As the Ce^{3+} centroid shift is a key parameter in the construction of an energy level scheme, it is only possible to utilize Eq. 4 if Ce^{3+}, Eu^{3+} and Eu^{2+} reside on the same crystallographic site. Furthermore, Eq. 14 and 16 are only valid if Ln^{3+} and Ln^{2+} ions reside on the same site. The assumed equality for redshifts and Stokes shifts for all ions with the same oxidation state only holds if all ions with the same valence incorporate equally.

In[134], the first empirical energy level scheme for two nonequivalent lattice sites was published, completely in agreement with the chemical shift model. This could be done thanks to site selective spectroscopy for both the Ce^{3+} and Eu^{2+} ions in the $SrAl_2O_4$ host[134,159]. Energy level modeling for multiple nonequivalent sites in the same host offers the boundary conditions that the host's VB and CB should be consistently located with respect to the vacuum level for each energy level scheme. This was

exploited to identify the CT excitation band of $SrAl_2O_4$:Eu^{3+} [134].

The possibility that unwanted impurity phases are formed should always be ruled out. Though experimentally controlling the purity of synthesized materials appears to be standard practice, overlooking - possibly luminescent - impurities can happen. In the case of the $ZnGa_2S_4$ host for example, multiple authors reported on the incorporation and luminescence of Eu^{2+} [4,160–165]. It was only 20 years after the first report that it was resolved by a combination of analytical techniques that small amounts of $EuGa_2S_4$ were causing the luminescence [166].

6 Roads for improvement

This section contains a brief summary of the error assessment, by enumerating the assets as well as pinpointing the frontiers where improvements are desirable.

The greatest advantage of using empirical rules prior to theoretical frameworks is certainly their simplicity in use, requiring paper and pencil rather than supercomputers. The lanthanides are in a way special because of their chemical similarity across the series. This ensures that a predictable behavior emerges and empirical rules can be found at all. This is especially visible if the trends for CT energies and $4f^N$-$4f^{N-1}5d^1$ transition energies are examined. These energies can consequently be calculated within a reasonable error margin for all other lanthanides on the same lattice site once the properties of one ion are known.

In the next step, host and vacuum referred energy levels schemes ought to be constructed. Multiple problems emerge along the way, diminishing the accuracy of the resulting parameters and energy level schemes. The bottleneck turns out to be related to the host's collective excitations. Even though it is desirable, there is no straightforward connection between the band gap of a material and the binding energy of self-trapped excitons. Together with the inaccurate way to determine the optical band gap experimentally, the CB bottom can only be positioned within a single standard deviation of 300 meV, i.e. errors of 0.5 eV are not uncommon.

Phenomena in which both the luminescent ion and the host find themselves in an excited state are thus notoriously difficult to predict or quantify. Even qualitative interpretation is not always clear. Examples are thermal quenching of luminescence, anomalous luminescence, IVCT, trapping and detrapping of charge carriers. In this context, it is appropriate to mention the distinction between a self-trapped and an impurity trapped exciton (ITE), the former being exclusively host related, the latter being related to the host and dopant simultaneously. The latter is suspected to be responsible or at least involved in the enumerated phenomena. A clear theory for all these phenomena does not exist at this moment. Possibly, a better understanding of these excited states is necessary before progress can be made from the empirical point of view.

The involvement of the $4f^{N-1}6s^1$ configuration in the formation

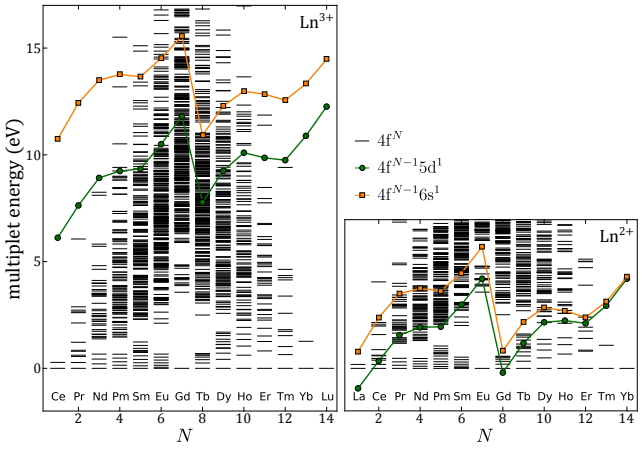

Fig. 9 Extended Dieke diagram for the Ln^{3+} and Ln^{2+} ions. The lowest spin allowed (with respect to the ground state) $4f^{N-1}5d^1$ and $4f^{N-1}6s^1$ levels are indicated by the zig-zag lines. A detailed account for the Ln^{3+} $4f^N$ levels is given in [169], the Ln^{2+} $4f^N$ levels were calculated by rescaling of radial integrals according to [86], the locations of the lowest $4f^{N-1}5d^1$ levels were taken from [48]. The locations of the lowest $4f^{N-1}6s^1$ levels are compiled in the supplementary information.

of states with impurity trapped exciton character was evidenced from first principles calculations for the Yb^{2+} ($N = 14$) ion in $SrCl_2$ [137]. Similar calculations showed that the ITE character in Cs_2GeF_6:U^{4+} originates from the $5f^17s^1$ configuration [167]. This suggests that empirically modeling the $4f^{N-1}6s^1$ configuration can ameliorate the understanding and predictability of the excited state dynamics in lanthanide materials. The possibility to model $4f^N n\ell^1$ configurations with the same machinery used to describe the $4f^{N-1}5d^1$ configuration was suggested by Thiel in 2003 [86]. It was theoretically verified from relativistic first principles calculations of trivalent lanthanides in the Cs_2NaYCl_6 host that Dorenbos' model for the $4f^{N-1}5d^1$ manifold can be extended to the $4f^{N-1}6s^1$ manifold [168]. In 2012, this was done for the first time for the K_3YF_6 host, based on the experimental spectra of Ce^{3+} and Tb^{3+} [60]. Fig. 9 shows the energy levels of the free Ln^{Q+} ions with the approximate locations of the lowest $4f^{N-1}6s^1$ states included. As can be seen, for Yb^{2+} the $4f^{N-1}5d^1$ and $4f^{N-1}6s^1$ manifolds have very similar energies, supporting the result of [137]. In practice it is more difficult to apply the model due to the obscuring of $4f^N$-$4f^{N-1}6s^1$ transitions by $4f^N$-$4f^{N-1}5d^1$ and CT transitions in excitation spectra.

A first attempt to extend this kind of empirical modeling towards other regions of the periodic table has already been undertaken. Rogers and Dorenbos gathered data to extend the chemical shift model to transition metal ions with a nd^1 ground state configuration (n = 3, 4, 5) [170–172]. Positive correlations showed up, however with an accuracy which is worse than for similar rules for the lanthanides, standard errors being typically of the order of 0.5 eV. The reason for this is at least twofold. First, the absence of chemical similarity in transition metals - since the spectroscopically active nd electrons are also involved in chemical bonding - makes the quest for trends intrinsically harder. Secondly, lanthanide spectroscopy was used to obtain the

location of the host's bands with respect to the vacuum level, leading to a considerable error from the start [170–172].

Notwithstanding the difficulties, empirical models are very useful tools for the interpretation of metal ion spectra and as a basis for more sophisticated investigations of individual cases. Given the associated accuracies, enumerated in the above text, theoretically designing functional materials within the stringent specifications of industry is still a challenge for empirical modeling.

7 Application: $CaGa_2S_4$:Ln^{Q+}

In this part, the energy level modeling and error analysis is explicitly applied to lanthanide doped calcium thiogallate $CaGa_2S_4$. This will allow assessing to which extent these models can be used for predicting spectroscopic properties. Sulfides form an interesting class of host materials for energy level modeling due to their small band gap energy, allowing to measure charge transfer and fundamental absorption bands within the limits of standard experimental equipment, i.e. without the need for VUV spectroscopy.

The polymorph with the orthorhombic crystal structure, corresponding to space group Fddd, is considered [173]. Although three nonequivalent alkaline earth metal sites are present on which the lanthanide dopants can incorporate, their shapes and sizes differ barely such that it can be safely assumed that only one alkaline earth metal site is present. This is underpinned by the narrow emission band of the Eu^{2+} ion (see further). The D_2 (or C_2) site symmetry can be approximated by a (non-crystallographic) D_{4d} point symmetry since the coordination polyhedra deviate only minimally from an idealized square antiprism [173]. In the strong-field coupling scheme, a single d electron with a fivefold degenerate energy level is expected to split in a singlet and two doublets.

7.1 Experimental spectra

Fig. 10 shows the emission and excitation spectra of Eu^{2+}, Ce^{3+} and Tm^{3+} in the described host material. The numerical values of the parameters that can be obtained from these measurements are summarized in Table 1. For band maxima, an experimental error of 20 meV was taken into account. To obtain the transition energy from the $4f^7(^8S_{7/2})$ ground state to the lowest $4f^6(^7F_0)5d^1$ state of Eu^{2+}, the point where the excitation band is 20% of its maximum value is usually taken. For this procedure, an experimental error of 50 meV is adopted. The error on empirical parameters that are regarded as constants, such as $E^{fd}(Ln^{Q+}, free)$ is taken to be 10 meV.

The Eu^{2+} and Ce^{3+} spectra are characterized by broadband luminescence in the visual range, coming from the intraconfigurational 5d-4f transition. Tm^{3+} shows line emission, originating from interconfigurational $4f^{12}$ transitions. The emission can be efficiently excited by a charge transfer transition, yielding a broad band in the UV range of the excitation spectrum. In the $CaGa_2S_4$:Tm^{3+} excitation spectrum, an additional band peaking at 4.43 eV is visible. A similar band was also reported elsewhere

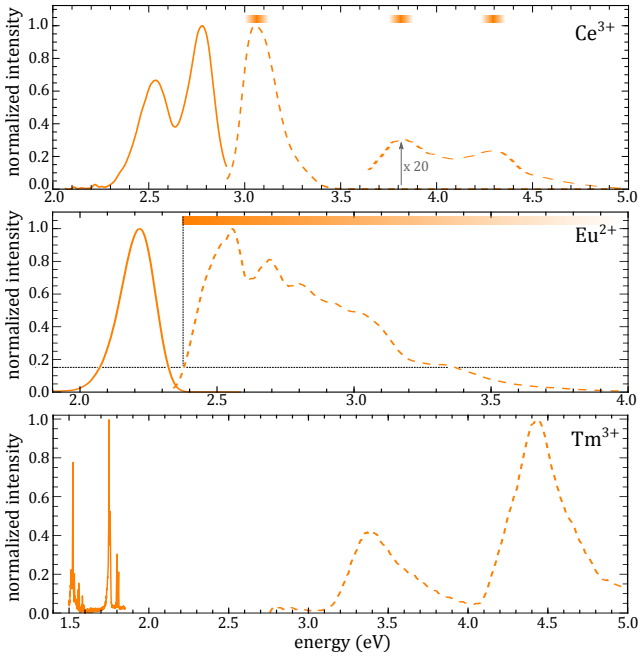

Fig. 10 Emission (solid lines) and excitation spectra (dashed lines) of lanthanide doped $CaGa_2S_4$, measured at 75 K. Top: Ce^{3+} doped, emission spectrum upon 410 nm (3.02 eV) excitation, excitation spectrum for 445 nm (2.79 eV) emission. Middle: Eu^{2+} doped, emission spectrum upon 450 nm (2.76 eV) excitation, excitation spectrum for 560 nm (2.21 eV) emission. Bottom: Tm^{3+} doped, emission spectrum upon 370 nm (3.35 eV) excitation, excitation spectrum for 810 nm (1.53 eV) emission.

and ascribed to fundamental absorption in the host material, sensitizing the Tm^{3+} emission [53].

7.2 Energy level scheme, construction and discussion

The complete lanthanide energy level scheme for $CaGa_2S_4$ is displayed in Fig. 11. In this figure, error margins are indicated, based on the error analysis in the previous paragraph, corresponding with single standard deviations and 68% prediction limits.

In Fig. 11, the deviations between the calculated and measured CT energy are displayed in a bar diagram for both types of calculations, i.e. from $\overline{\Delta E}$ parameters and from the contraction tilt parameters ($\alpha(2, CaGa_2S_4) = 0.109 eV/pm$ and $\alpha(3, CaGa_2S_4) = 0.175 eV/pm$). The typical error lies within 0.5 eV, corresponding to twice the calculated standard deviation. A better correspondence was found for the CT energies when the average $\overline{\Delta E}$ parameters were used. The difference in CT energies between these two approaches amounts up to a few 100 meV.

From the point of view of error analysis, no larger deviation is a priori expected for the CT energies obtained from the contraction tilt than those obtained from the $\overline{\Delta E}$s. Nevertheless, it appears to be the case. A possible reason for this is the inability to describe the detailed interactions in the lanthanide defect cluster with the main premise of the chemical shift model, namely the Coulomb potential, Eq. A3. In this case, Eq. A9 does not furnish the correct

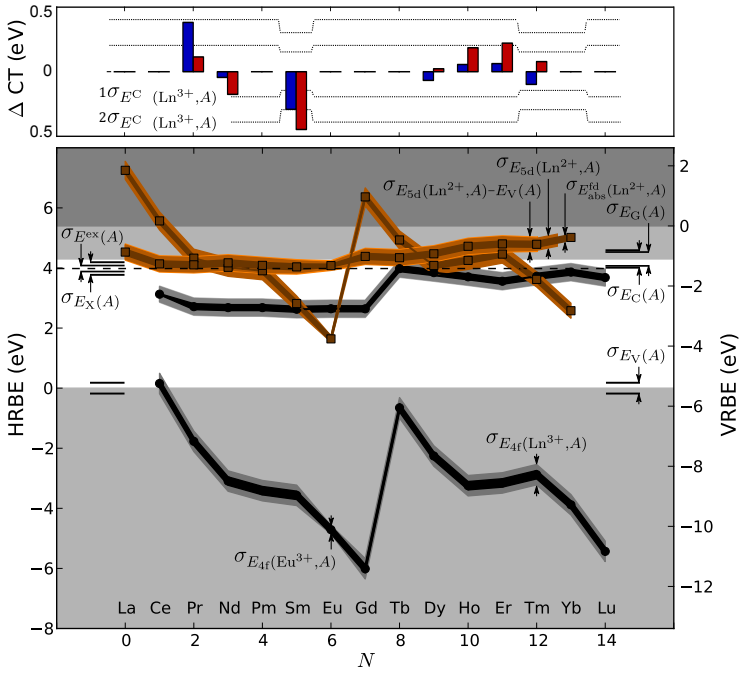

Fig. 11 Lanthanide impurity energy level scheme for the $CaGa_2S_4$ ($A = CaGa_2S_4$) host, calculated with the $\overline{\Delta E}$ parameters. The saw tooth shaped (zig-zag) curves represent the lowest $4f^N$ level of the ion, the more or less horizontal lines the lowest $4f^{N-1}5d^1$ level. Orange squares for divalent lanthanide ions, black circles for trivalent lanthanide ions. The single standard deviations, σ, for the lowest $4f^N$ and $4f^{N-1}5d^1$ levels are represented by the thickness of the lines, the errors on the location of the host's VB, CB and exciton binding energy are indicated at the left and right sides of the figure. The symbol of the quantity of which the standard deviation is shown, is denoted in the subscript. The differences between the calculated and experimentally determined CT energies (ΔCT) are represented in the bar diagram on top. Blue for CT energies calculated from the averaged $\overline{\Delta E}$s, red for CT energies, calculated from the contraction tilt parameters α. When multiple experimental energies were available, the average was calculated [52,53].

relation between $\alpha(Q,A)$ and $E_{4f}^{chem}(Eu^{Q+},A)$. Alternatively, a simple rotation as described by Eq. 7 - which remains valid for a more general class of models than the chemical shift model - might be insufficient to describe the change of shape of the 4f curves upon incorporation. After all, the 4f curves obtained with $\overline{\Delta E(Ln,Eu,Q)}$ can not be obtained by simple rotation of $\Delta E(Ln,Eu,Q,free)$, the optimal contraction tilt parameters of $\alpha(2,\overline{A}) = 0.097eV/pm$ and $\alpha(3,\overline{A}) = 0.156eV/pm$ yield some deviations.

If the energy level scheme (Fig. 11) is compared with the one available in literature ([53]), a few differences show up. In Fig. 11, most Ln^{2+} $4f^{N-1}5d^1$ states are within the conduction band while they are below in [53]. This can be attributed to the different E^{ex} values used in both calculations. Bessière et al. used the maximum of a host related excitation band in the spectrum of Ce^{3+} [53]. It is however not sure whether the maximum of the broad excitation band corresponds with self-trapped exciton creation. Furthermore, the Coulomb correlation energy in [53] is rather low (around 5.5 eV according to Fig. 5), corresponding with the value for Eu metal, recorded by Dorenbos (Fig. 4 and [94]). This results in a Ln^{3+} 4f curve which is too loosely bound with respect to the vacuum, having the Tb^{3+} 4f state in the band gap while in Fig. 11 it lies in the VB. This deviation can be related to the less extended energy level model used 10 years ago. On the other hand, if one considers realistic errors on all calculated quantities, the differences between both energy level schemes are limited and the scheme of Bessière et al. can be used as well. From the energy level scheme, electronic and optical properties of $CaGa_2S_4$:Ln^{Q+} are predicted.

From the locations of the $4f^N$ levels, it is inferred that the europium ion will be divalently incorporated, matching observation. All other lanthanides except for ytterbium are expected to be trivalent. Ytterbium is a more difficult case as the Yb^{2+} $4f^N$ ground state is very close to the center of the band gap. Comparison with other sulfide hosts suggests that ytterbium will most likely be incorporated as Yb^{2+} [135].

Afterglow of a few seconds has been reported in $CaGa_2S_4$:Eu^{2+} when this phosphor is co-doped with another lanthanide ion [174–176]. The locations of the lowest Ln^{2+} 4f states with respect to the host's conduction band are of particular interest since it has been suggested that Ln^{3+} ions behave as electron acceptors, trapping auto-ionized electrons from the light emitting ion [132]. This has been successfully demonstrated for YPO_4:Ce^{3+}, Ln^{3+}, where trap depths between 0.5 eV and 3.2 eV were found from thermoluminescence (TL) spectroscopy [133]. In the case of $CaGa_2S_4$ however, the lowest 4f states of Pr^{2+}, Nd^{2+}, Gd^{2+}, Dy^{2+}, Ho^{2+} and Er^{2+} lie very close or inside the conduction band of $CaGa_2S_4$. For this reason, all these lanthanides are expected to be poor trapping centers and no meaningful trend

is expected as a function of N. This is also reflected in Figure 7 of[176] where three trap levels were fitted to TL glow peaks. The observed traps might be rather coming from defect levels, other than those associated with the 4f electrons of the codopant, nonetheless potentially caused by the incorporation of the codopant. For Sm^{3+} and Tm^{3+} as codopant, no light emission was observed which is in accordance with the calculated trap depths of 1.48 ± 0.31 eV and 0.68 ± 0.23 eV respectively, calculated with respect to the conduction band bottom. In these cases, the afterglow will be obscured by the deep traps from the Tm^{3+} and Sm^{3+} acceptor ions, which cannot be emptied at room temperature within a reasonable time. If the trap depths are calculated with respect to the self-trapped exciton binding energy, one obtains 1.16 ± 0.24 eV and 0.36 ± 0.10 eV for Sm^{3+} and Tm^{3+}. The error on the trap depth for Tm^{3+} is smaller thanks to the fact that the Tm^{3+} CT was used to position the VB. The predicitive power of these trap depths is limited due to the large error margin. A trap of depth 0.68 ± 0.23 eV for example can be both too shallow for efficient charge storage, perfect for gradual charge release to construct persistent luminescent materials or too deep to be emptied at room temperature.

8 Conclusions

This work featured an extensive discussion on the empirical modeling of luminescent lanthanide materials. The fundamental relationships of the model were devised by multiple authors during the last 40 years and extensively reviewed and fine-tuned by Dorenbos during the last 20 years through data mining and revisiting of scientific literature on lanthanide materials.

The different empirical relationships of the model were reviewed as well as the necessary steps to build an energy level scheme from spectroscopic measurements. A profound analysis was performed on the accumulated errors. The errors are not only determined for the energy level scheme itself, but also for the commonly derived physical observables.

Table 1 Optical properties of Ce^{3+}, Eu^{2+} and Tm^{3+} ions in the $CaGa_2S_4$ host. These parameters serve as input for the calculation of the lanthanide energy level schemes. d_1, d_2 and d_3 denote the positions of the three 4f-5d excitation bands of Ce^{3+}, f_1 and f_2 denote the positions of the two 5d-4f emission bands of Ce^{3+}. All values in eV.

Optical band gap $E^{ex}(A)$		3.98 ± 0.10
Ce^{3+}	Absorption $E_{abs}^{fd_1}(Ce^{3+},A)$	3.05 ± 0.02
	Absorption $E_{abs}^{fd_2}(Ce^{3+},A)$	3.81 ± 0.02
	Absorption $E_{abs}^{fd_3}(Ce^{3+},A)$	4.29 ± 0.02
	Redshift $D(Ce^{3+},A)$	3.07 ± 0.03
	Centroid shift $\varepsilon_c(Ce^{3+},A)$	2.50 ± 0.02
	Crystal field splitting $\varepsilon_{cfs}(Ce^{3+},A)$	1.24 ± 0.03
	Emission $E_{em}^{f_1d}(Ce^{3+},A)$	2.54 ± 0.02
	Emission $E_{em}^{f_2d}(Ce^{3+},A)$	2.78 ± 0.02
	Stokes shift $\Delta S(Ce^{3+},A)$	0.27 ± 0.03
Eu^{2+}	Redshift $D(Eu^{2+},A)$	1.83 ± 0.05
	Stokes shift $\Delta S(Eu^{2+},A)$	0.17 ± 0.06
Tm^{3+}	Charge transfer $E^{CT}(Tm^{3+},A)$	3.37 ± 0.02

The error analysis revealed that a different accuracy is obtained when the energy level locations are calculated with respect to the vacuum or to the host's valence or conduction bands. The lowest 4f and the 5d states of the divalent and trivalent lanthanide ions can be probed with a standard deviation of respectively 100-150 meV and 250-300 meV with respect to the vacuum level. If referred to the valence band, the standard deviations are typically 50 meV higher.

The conduction band bottom can only be positioned within a standard deviation of 300 meV. Not only can the optical band gap be determined in a rather loose way from diffuse reflection spectroscopy, but also the empirical relationship for calculating the self-trapped exciton binding energy proves to be inaccurate, yielding relative errors up to 100% for materials with a small band gap energy. This has its repercussions on the accuracy of quantities describing phenomena in which conduction band states are reckoned to be involved such as thermal quenching, electron transfer or anomalous luminescence. The model does not allow to quantitatively describe these phenomena. Nevertheless, correlations which are revealed by the model remain valid and allow for qualitative interpretation of experiments.

In the second part of the manuscript, an energy level scheme was devised for $CaGa_2S_4$ based on optical spectroscopy of Ce^{3+}, Eu^{2+} and Tm^{3+}. The comparison between calculated and measured quantities is in accordance with the prior error analysis and the energy level schemes allowed for a better understanding of new and already reported results on these materials.

Acknowledgements

JJJ thanks the agency for Innovation by Science and Technology (IWT) for a research grant (121024). PFS and DP are grateful to the IWT for a SBO-IWT grant (SBO130030).

A Thiel-Dorenbos parameterization of the chemical shift

Thiel parameterized the chemical shift as originating from the electrostatic, i.e. Madelung, interaction of the ions of the host crystal with the dopant ion, complemented with a term, correcting for the relaxation (α) of the lattice due to the non-equal ionic radii (R) of the lanthanide dopant (Ln^{Q+}) and the metal ion ($M^{Q'+}$) which site it occupies[84–87]:

$$E_{4f}^{chem}(Ln^{Q+},A) = \frac{Qe^2}{4\pi\varepsilon_0 d(A)} M(A) + \alpha(Q,A)\Delta R(Ln^{Q+},A). \quad (A1)$$

Herein, $M(A)$ is the Madelung constant corresponding with the crystal lattice site on which the lanthanide incorporates and d the bond length to the nearest neighbors in the undoped crystal. ΔR is the difference in ionic radii between the dopant and the metal ion on which site the dopant resides:

$$\Delta R(Ln^{Q+},A) = R(Ln^{Q+}) - R(M^{Q'+}). \quad (A2)$$

In Dorenbos' model, the chemical shift is rationalized as the energy resulting from an electrostatic interaction between a single 4f electron and a charge at a certain *screening distance* ($R_Q(\mathrm{Ln}^{Q+},A)$) described by a Coulomb-like law[88]:

$$E_{4f}^{\mathrm{chem}}(\mathrm{Ln}^{Q+},A) = \frac{Qe^2}{4\pi\varepsilon_0 R_Q(\mathrm{Ln}^{Q+},A)} \quad (A3)$$

$$= \frac{Qe^2}{4\pi\varepsilon_0 R_Q(\mathrm{Eu}^{Q+},A)}$$

$$+ \alpha(Q,A)\left[\Delta R(\mathrm{Ln}^{Q+},A) - \Delta R(\mathrm{Eu}^{Q+},A)\right] + \ldots$$

where a series expansion was applied around the case of the europium ion and a linear relationship utilized for the screening distance across the lanthanide series:

$$R_Q(\mathrm{Ln}^{Q+},A) = R_Q(\mathrm{Eu}^{Q+},A) - f\left[R(\mathrm{Ln}^{Q+}) - R(\mathrm{Eu}^{Q+})\right]. \quad (A4)$$

Herein, f represents the extent of mechanical lattice deformation upon incorporation of impurity ions. It is assumed to be independent of both host lattice and dopant ion[88].

As one can see from Eqs. A2 and A3, both models are equivalent up to linear order in series expansion of Eq. A3, the former without a lanthanide as reference, the latter with europium as the lanthanide of reference (i.e. the last line of Eq. A3 vanishes for Ln=Eu).

The equivalence of the α parameters in the chemical shift models of Thiel and Dorenbos can be shown by explicitly writing the chemical shift for Eu^{Q+}:

$$E_{4f}^{\mathrm{chem,T.}}(\mathrm{Eu}^{Q+},A) = \frac{Qe^2}{4\pi\varepsilon_0 d(A)} M(A) + \alpha_{\mathrm{T}}(Q,A)\Delta R(\mathrm{Eu}^{Q+},A) \quad (A5)$$

$$E_{4f}^{\mathrm{chem,D.}}(\mathrm{Eu}^{Q+},A) = \frac{Qe^2}{4\pi\varepsilon_0 R_Q(\mathrm{Eu}^{Q+},A)} \quad (A6)$$

Where T and D denote Thiel and Dorenbos respectively. If Eq. A5 and A6 are respectively subtracted from A2 and A3, one obtains $E_{4f}^{\mathrm{chem}}(\mathrm{Ln}^{Q+},A) - E_{4f}^{\mathrm{chem}}(\mathrm{Eu}^{Q+},A)$ for both models. These ought to be equal:

$$\alpha_{\mathrm{T}}(Q,A)\left[R(\mathrm{Ln}^{Q+}) - R(\mathrm{M}^{Q'+})\right] - \alpha_{\mathrm{T}}(Q,A)\left[R(\mathrm{Eu}^{Q+}) - R(\mathrm{M}^{Q'+})\right]$$

$$= \alpha_{\mathrm{D}}(Q,A)\left[R(\mathrm{Ln}^{Q+}) - R(\mathrm{Eu}^{Q+})\right], \quad (A7)$$

indeed yielding $\alpha_{\mathrm{T}}(Q,A) = \alpha_{\mathrm{D}}(Q,A)$. The subscripts T and D can thus be omitted.

The screening distance $R_Q(\mathrm{Eu}^{Q+},A)$, introduced by Dorenbos, is then related to the Madelung constant:

$$\frac{1}{R_Q(\mathrm{Eu}^{Q+},A)} = \frac{M(A)}{d(A)} + \frac{4\pi\varepsilon_0\alpha(Q,A)}{Qe^2}\Delta R(\mathrm{Eu}^{Q+},A). \quad (A8)$$

The binding energy shift per unit change in ionic radius, α, is named the contraction tilt parameter by Dorenbos. Referring to the decreasing ionic radius for increasing atomic number for lanthanides, it is also commonly known as the lanthanide contraction[88].

Both authors state that the chemical shift model should be approached in an empirical way, i.e. by making abstraction of an exact meaning of the M (or R_Q) and α parameters, but rather regard them as effective parameters. In this way the model can describe more complex interactions than purely the electrostatic one. Thiel considered M and α as two independent parameters which can be fitted to experimental photoelectron spectroscopy (PES) spectra. Dorenbos considers Eq. A2 as an approximation of A3, restricting the number of independent parameters to one. In this case, α can be calculated as:

$$\alpha(Q,A) = \frac{Qe^2 f}{4\pi\varepsilon_0 R_Q^2(\mathrm{Eu}^{Q+},A)} = \frac{4\pi\varepsilon_0 f}{Qe^2}\left[E_{4f}^{\mathrm{chem}}(\mathrm{Eu}^{Q+},A)\right]^2 \quad (A9)$$

In reality, the choice to use one or two parameters in the chemical shift model is of no relevance because the chemical shift is usually determined from another, purely empirical relationship (Eq. 5, see §4.1).

References

1 M. H. Crawford, *Ieee Journal of Selected Topics in Quantum Electronics*, 2009, **15**, 1028–1040.
2 P. F. Smet, A. B. Parmentier and D. Poelman, *Journal of the Electrochemical Society*, 2011, **158**, R37–R54.
3 S. Ye, F. Xiao, Y. X. Pan, Y. Y. Ma and Q. Y. Zhang, *Materials Science & Engineering R-Reports*, 2010, **71**, 1–34.
4 H. A. Hoppe, *Angewandte Chemie-International Edition*, 2009, **48**, 3572–3582.
5 M. L. Saladino, D. C. Martino, M. A. Floriano, D. Hreniak, L. Marciniak, W. Strek and E. Caponetti, *Journal of Physical Chemistry C*, 2014, **118**, 9107–9113.
6 W. Z. Lv, Y. C. Jia, Q. Zhao, W. Lu, M. M. Jiao, B. Q. Shao and H. P. You, *Journal of Physical Chemistry C*, 2014, **118**, 7250–7250.
7 X. M. Liu, Y. Lu, C. Chen, S. L. Luo, Y. H. Zeng, X. Q. Zhang, M. M. Shang, C. X. Li and J. Lin, *Journal of Physical Chemistry C*, 2014, **118**, 27516–27524.
8 R.-J. Xie, N. Hirosaki and T. Takeda, *Applied Physics Express*, 2009, **2**, 022401.
9 G. Harbers, S. J. Bierhuizen and M. R. Krames, *Journal of Display Technology*, 2007, **3**, 98–109.
10 A. Jha, B. Richards, G. Jose, T. Teddy-Fernandez, P. Joshi, X. Jiang and J. Lousteau, *Progress in Materials Science*, 2012, **57**, 1426–1491.
11 P. Leblans, D. Vandenbroucke and P. Willems, *Materials*, 2011, **4**, 1034–1086.
12 F. Loncke, H. Vrielinck, P. Matthys, F. Callens, J. P. Tahon and P. Leblans, *Spectrochimica Acta Part a-Molecular and Biomolecular Spectroscopy*, 2008, **69**, 1322–1326.

13 H. Vrielinck, F. Loncke, J. P. Tahon, P. Leblans, P. Matthys and F. Callens, *Physical Review B*, 2011, **83**, 054102.

14 V. Jary, M. Nikl, S. Kurosawa, Y. Shoji, E. Mihokova, A. Beitlerova, G. P. Pazzi and A. Yoshikawa, *Journal of Physical Chemistry C*, 2014, **118**, 26521–26529.

15 J. Brubach, C. Pflitsch, A. Dreizler and B. Atakan, *Progress in Energy and Combustion Science*, 2013, **39**, 37–60.

16 V. Lojpur, Z. Antic and M. D. Dramicanin, *Physical Chemistry Chemical Physics*, 2014, **16**, 25636–25641.

17 K. W. Meert, V. A. Morozov, A. M. Abakumov, J. Hadermann, D. Poelman and P. F. Smet, *Optics Express*, 2014, **22**, A961–A972.

18 L. Zhang, C. Xu and H. Yamada, *IOP Conference Series: Materials Science and Engineering*, 2011, **18**, 212001.

19 J. Botterman, K. Van den Eeckhout, I. De Baere, D. Poelman and P. F. Smet, *Acta Materialia*, 2012, **60**, 5494–5500.

20 K. Van den Eeckhout, P. F. Smet and D. Poelman, *Materials*, 2010, **3**, 2536–2566.

21 K. Van den Eeckhout, D. Poelman and P. F. Smet, *Materials*, 2013, **6**, 2789–2818.

22 H. F. Brito, J. Holsa, T. Laamanen, M. Lastusaari, M. Malkamaki and L. C. V. Rodrigues, *Optical Materials Express*, 2012, **2**, 371–381.

23 L. C. V. Rodrigues, H. F. Brito, J. Holsa, R. Stefani, M. C. F. C. Felinto, M. Lastusaari, T. Laamanen and L. A. O. Nunes, *Journal of Physical Chemistry C*, 2012, **116**, 11232–11240.

24 H. Bethe, *Annalen der Physik*, 1929, **395**, 133–208.

25 J. H. Van Vleck, *Physical Review*, 1932, **41**, 208–215.

26 M. Dolg, *Computational Methods in Lanthanide and Actinide Chemistry*, Wiley, 2015.

27 M. Atanasov, D. Ganyushin, K. Sivalingam and F. Neese, *Molecular Electronic Structures of Transition Metal Complexes*, 2012, **143**, 149–220.

28 D. Y. Zhai, L. X. Ning, Y. C. Huang and G. K. Liu, *Journal of Physical Chemistry C*, 2014, **118**, 16051–16059.

29 Z. Barandiaran and L. Seijo, *Journal of Chemical Physics*, 2013, **138**, 074102.

30 L. Seijo and Z. Barandiaran, *Physical Chemistry Chemical Physics*, 2013, **15**, 19221–19231.

31 L. Seijo and Z. Barandiaran, *Optical Materials*, 2013, **35**, 1932–1940.

32 L. Seijo and Z. Barandiaran, *Physical Chemistry Chemical Physics*, 2014, **16**, 3830–3834.

33 M. Krosnicki, A. Kedziorski, L. Seijo and Z. Barandiaran, *Journal of Physical Chemistry A*, 2014, **118**, 358–368.

34 J. L. Pascual, Z. Barandiaran and L. Seijo, *Journal of Luminescence*, 2014, **145**, 808–817.

35 A. J. Cohen, P. Mori-Sanchez and W. T. Yang, *Chemical Reviews*, 2012, **112**, 289–320.

36 A. Canning, A. Chaudhry, R. Boutchko and N. Gronbech-Jensen, *Physical Review B*, 2011, **83**, 125115.

37 S. Derenzo, G. Bizarri, R. Borade, E. Bourret-Courchesne, R. Boutchko, A. Canning, A. Chaudhry, Y. Eagleman, G. Gundiah, S. Hanrahan, M. Janecek and M. Weber, *Nuclear Instruments & Methods in Physics Research Section a-Accelerators Spectrometers Detectors and Associated Equipment*, 2011, **652**, 247–250.

38 A. Chaudhry, R. Boutchko, S. Chourou, G. Zhang, N. Gronbech-Jensen and A. Canning, *Physical Review B*, 2014, **89**, 155105.

39 M. Atanasov and C. Daul, *Chimia*, 2005, **59**, 504–510.

40 M. Atanasov and C. A. Daul, *Comptes Rendus Chimie*, 2005, **8**, 1421–1433.

41 C. E. Schäffer, C. Anthon and J. Bendix, *Coordination Chemistry Reviews*, 2009, **253**, 575–593.

42 H. Ramanantoanina, W. Urland, A. Garcia-Fuente, F. Cimpoesu and C. Daul, *Chemical Physics Letters*, 2013, **588**, 260–266.

43 H. Ramanantoanina, W. Urland, F. Cimpoesu and C. Daul, *Physical Chemistry Chemical Physics*, 2013, **15**, 13902–13910.

44 H. Ramanantoanina, W. Urland, A. Garcia-Fuente, F. Cimpoesu and C. Daul, *Physical Chemistry Chemical Physics*, 2014, **16**, 14625–14634.

45 L. Gonzalez, D. Escudero and L. Serrano-Andres, *Chemphyschem*, 2012, **13**, 28–51.

46 A. Domingo, M. A. Carvajal, C. de Graaf, K. Sivalingam, F. Neese and C. Angeli, *Theoretical Chemistry Accounts*, 2012, **131**, 1234.

47 M. Roemelt and F. Neese, *Journal of Physical Chemistry A*, 2013, **117**, 3069–3083.

48 P. Dorenbos, *ECS Journal of Solid State Science and Technology*, 2013, **2**, R3001–R3011.

49 M. Nazarov, D. Y. Noh and H. Kim, *Materials Chemistry and Physics*, 2008, **107**, 456–464.

50 M. Nazarov, B. Tsukerblat and D. Y. Noh, *Journal of Luminescence*, 2008, **128**, 1533–1540.

51 P. F. Smet, I. Moreels, Z. Hens and D. Poelman, *Materials*, 2010, **3**, 2834–2883.

52 A. Garcia, F. Guillen and C. Fouassier, *Journal of Luminescence*, 1985, **33**, 15–27.

53 A. Bessiere, P. Dorenbos, C. W. E. van Eijk, E. Yamagishi, C. Hidaka and T. Takizawa, *Journal of the Electrochemical Society*, 2004, **151**, H254–H260.

54 J. Griffith, *The Theory of Transition-metal Ions*, Cambridge University Press, 1961.

55 B. Wybourne, *Spectroscopic properties of rare earths*, Interscience Publishers, 1965.

56 C. Görller-Walrand and K. Binnemans, in *Rationalization of crystal-field parameterization*, ed. K. A. Gschneidner and L. Eyring, North-Holland, 1996, vol. 23, book section 155.

57 L. S. Hu, M. F. Reid, C. K. Duan, S. D. Xia and M. Yin, *Journal of Physics-Condensed Matter*, 2011, **23**, 045501.

58 C. G. Ma, M. F. Reid, C. K. Duan, S. D. Xia and M. Yin, *Journal of Rare Earths*, 2007, **25**, 262–267.

59 C. G. Ma, C. K. Duan, S. D. Xia, M. Yin and M. F. Reid, *Journal of Physics and Chemistry of Solids*, 2008, **69**, 2578–2583.

60 C. G. Ma, M. G. Brik, W. Ryba-Romanowski, H. C. Swart and

M. A. Gusowski, *Journal of Physical Chemistry A*, 2012, **116**, 9158–9180.
61 C. G. Ma, M. G. Brik, V. Kiisk and I. Sildos, *Journal of Luminescence*, 2013, **133**, 39–44.
62 K. Kikoin and V. Fleurov, *Transition Metal Impurities in Semiconductors: Electronic Structure and Physical Properties*, World Scientific, 1994.
63 G. F. Koster and J. C. Slater, *Physical Review*, 1954, **95**, 1167–1176.
64 G. F. Koster and J. C. Slater, *Physical Review*, 1954, **96**, 1208–1223.
65 W. Kohn, *Physical Review*, 1957, **105**, 509–516.
66 S. T. Pantelides, *Reviews of Modern Physics*, 1978, **50**, 797–858.
67 J. Callaway, *Quantum Theory of the Solid State*, Elsevier Science, 2013.
68 J. Callaway and A. J. Hughes, *Physical Review*, 1967, **156**, 860–876.
69 F. D. M. Haldane and P. W. Anderson, *Physical Review B*, 1976, **13**, 2553–2559.
70 V. N. Fleurov and K. A. Kikoin, *Journal of Physics C-Solid State Physics*, 1976, **9**, 1673–1683.
71 G. Picoli, A. Chomette and M. Lannoo, *Physical Review B*, 1984, **30**, 7138–7147.
72 T. Koopmans, *Physica*, 1934, **1**, 104–113.
73 W. Dickhoff and D. Van Neck, *Many-body Theory Exposed!: Propagator Description of Quantum Mechanics in Many-body Systems*, World Scientific, 2005.
74 K. A. Kikoin and V. N. Fleurov, *Zhurnal Eksperimentalnoi I Teoreticheskoi Fiziki*, 1979, **77**, 1062–1075.
75 K. A. Kikoin and V. N. Fleurov, *Journal of Physics C-Solid State Physics*, 1984, **17**, 2357–2373.
76 C. Delerue and M. Lannoo, *Physical Review Letters*, 1991, **67**, 3006–3009.
77 S. Schmittrink, C. M. Varma and A. F. J. Levi, *Physical Review Letters*, 1991, **66**, 2782–2785.
78 M. Lannoo and J. Bourgoin, *Point Defects in Semiconductors I: Theoretical Aspects*, Springer Berlin Heidelberg, 1981.
79 C. Freysoldt, B. Grabowski, T. Hickel, J. Neugebauer, G. Kresse, A. Janotti and C. G. Van de Walle, *Reviews of Modern Physics*, 2014, **86**, 253–305.
80 L. Pauling, *Physical Review*, 1929, **34**, 954–963.
81 C. Pedrini, D. S. Mcclure and C. H. Anderson, *Journal of Chemical Physics*, 1979, **70**, 4959–4962.
82 D. S. Mcclure and C. Pedrini, *Journal De Physique*, 1985, **46**, 397–401.
83 C. Pedrini, F. Rogemond and D. S. Mcclure, *Journal of Applied Physics*, 1986, **59**, 1196–1201.
84 C. W. Thiel, H. Cruguel, H. Wu, Y. Sun, G. J. Lapeyre, R. L. Cone, R. W. Equall and R. M. Macfarlane, *Physical Review B*, 2001, **64**, 085107.
85 C. W. Thiel, H. Cruguel, Y. Sun, G. J. Lapeyre, R. M. Macfarlane, R. W. Equall and R. L. Cone, *Journal of Luminescence*, 2001, **94**, 1–6.
86 C. W. Thiel, *Thesis, http://scholarworks.montana.edu/xmlui/handle/1/2416*, Montana State University, 2003.
87 C. W. Thiel and R. L. Cone, *Journal of Luminescence*, 2011, **131**, 386–395.
88 P. Dorenbos, *Physical Review B*, 2012, **85**, 165107.
89 P. Dorenbos, *Journal of Alloys and Compounds*, 2002, **341**, 156–159.
90 P. Dorenbos, J. Andriessen and C. W. E. van Eijk, *Journal of Solid State Chemistry*, 2003, **171**, 133–136.
91 P. Boutinaud, E. Cavalli and M. Bettinelli, *Journal of Physics-Condensed Matter*, 2007, **19**, 386230.
92 A. H. Krumpel, P. Boutinaud, E. van der Kolk and P. Dorenbos, *Journal of Luminescence*, 2010, **130**, 1357–1365.
93 P. Dorenbos, *Journal of Luminescence*, 2013, **135**, 93–104.
94 P. Dorenbos, *Journal of Luminescence*, 2013, **136**, 122–129.
95 P. Dorenbos, *Physical Review B*, 2002, **65**, 235110.
96 J. Sugar and J. Reader, *Journal of Chemical Physics*, 1973, **59**, 2083–2089.
97 R. D. Shannon, *Acta Crystallographica Section A*, 1976, **32**, 751–767.
98 P. Dorenbos, *Journal of Physics-Condensed Matter*, 2003, **15**, 8417–8434.
99 P. Dorenbos, *Journal of Alloys and Compounds*, 2009, **488**, 568–573.
100 P. Dorenbos, A. H. Krumpel, E. van der Kolk, P. Boutinaud, M. Bettinelli and E. Cavalli, *Optical Materials*, 2010, **32**, 1681–1685.
101 M. Cardona and L. Ley, *Photoemission in solids: General principles*, Springer-Verlag, 1978.
102 P. Dorenbos, *Journal of Luminescence*, 2005, **111**, 89–104.
103 Y. Toyozawa, K. Song and R. Williams, *Self-Trapped Excitons*, Springer Berlin Heidelberg, 1996.
104 P. Dorenbos, *Ecs Journal of Solid State Science and Technology*, 2014, **3**, R19–R24.
105 P. Dorenbos, *Chemistry of Materials*, 2005, **17**, 6452–6456.
106 N. Ashcroft and N. Mermin, *Solid State Physics*, Cengage Learning, 2011.
107 M. R. MacDonald, J. E. Bates, J. W. Ziller, F. Furche and W. J. Evans, *Journal of the American Chemical Society*, 2013, **135**, 9857–9868.
108 M. R. MacDonald, M. E. Fieser, J. E. Bates, J. W. Ziller, F. Furche and W. J. Evans, *Journal of the American Chemical Society*, 2013, **135**, 13310–13313.
109 P. Dorenbos, *Journal of Luminescence*, 2000, **91**, 91–106.
110 C. K. Jørgensen, *Molecular Physics*, 1962, **5**, 271–277.
111 J. L. Ryan and C. K. Jørgensen, *Journal of Physical Chemistry*, 1966, **70**, 2845–2857.
112 M. J. J. Lammers and G. Blasse, *Journal of the Electrochemical Society*, 1987, **134**, 2068–2072.
113 P. Dorenbos, *Journal of Physics-Condensed Matter*, 2003, **15**, 575–594.
114 P. Dorenbos, *Journal of Luminescence*, 2003, **104**, 239–260.

115 P. Dorenbos, *Journal of Luminescence*, 2000, **91**, 155–176.

116 P. Dorenbos, *Journal of Physics-Condensed Matter*, 2003, **15**, 4797–4807.

117 J. J. Joos, K. W. Meert, A. B. Parmentier, D. Poelman and P. F. Smet, *Optical Materials*, 2012, **34**, 1902–1907.

118 T. L. Barry, *Journal of the Electrochemical Society*, 1968, **115**, 1181–1184.

119 B. Henderson and G. Imbusch, *Optical spectroscopy of inorganic solids*, Oxford University Press, Incorporated, 2006.

120 A. Zych, J. Ogieglo, C. Ronda, C. D. Donega and A. Meijerink, *Journal of Luminescence*, 2013, **134**, 174–179.

121 S. Leyre, E. Coutino-Gonzalez, J. J. Joos, J. Ryckaert, Y. Meuret, D. Poelman, P. F. Smet, G. Durinck, J. Hofkens, G. Deconinck and P. Hanselaer, *Review of Scientific Instruments*, 2014, **85**, 123115.

122 G. Blasse, W. Schipper and J. J. Hamelink, *Inorganica Chimica Acta*, 1991, **189**, 77–80.

123 M. Ando and Y. A. Ono, *Journal of Crystal Growth*, 1992, **117**, 969–974.

124 M. Raukas, S. A. Basun, W. vanSchaik, W. M. Yen and U. Happek, *Applied Physics Letters*, 1996, **69**, 3300–3302.

125 U. Happek, S. A. Basun, J. Choi, J. K. Krebs and M. Raukas, *Journal of Alloys and Compounds*, 2000, **303**, 198–206.

126 P. Dorenbos, *Journal of Physics-Condensed Matter*, 2005, **17**, 8103–8111.

127 W. B. Fowler and D. L. Dexter, *Physical Review*, 1962, **128**, 2154–2165.

128 S. H. M. Poort, A. Meyerink and G. Blasse, *Journal of Physics and Chemistry of Solids*, 1997, **58**, 1451–1456.

129 P. Dorenbos and E. G. Rogers, *ECS Journal of Solid State Science and Technology*, 2014, **3**, R150–R158.

130 P. Dorenbos, *Journal of Physics-Condensed Matter*, 2003, **15**, 2645–2665.

131 A. Lecointre, A. Bessiere, A. J. J. Bos, P. Dorenbos, B. Viana and S. Jacquart, *Journal of Physical Chemistry C*, 2011, **115**, 4217–4227.

132 P. Dorenbos, *Journal of the Electrochemical Society*, 2005, **152**, H107–H110.

133 P. Dorenbos, A. J. J. Bos, N. R. J. Poolton and F. T. You, *Journal of Luminescence*, 2013, **133**, 45–50.

134 J. Botterman, J. J. Joos and P. F. Smet, *Physical Review B*, 2014, **90**, 085147.

135 A. B. Parmentier, J. J. Joos, P. F. Smet and D. Poelman, *Journal of Luminescence*, 2014, **154**, 445–451.

136 G. Sanchez-Sanz, L. Seijo and Z. Barandiaran, *Journal of Chemical Physics*, 2010, **133**, 114506.

137 G. Sanchez-Sanz, L. Seijo and Z. Barandiaran, *Journal of Chemical Physics*, 2010, **133**, 114509.

138 G. Blasse and B. Grabmaier, in *Luminescent materials*, Springer-Verlag, 1994, book Appendix 4.

139 J. Mooney and P. Kambhampati, *The Journal of Physical Chemistry Letters*, 2014, **5**, 3497–3497.

140 W. Martin, R. Zalubas and L. Hagan, *Atomic energy levels–the rare-earth elements: the spectra of lanthanum, cerium, praseodymium, neodymium, promethium, samarium, europium, gadolinium, terbium, dysprosium, holmium, erbium, thulium, ytterbium, and lutetium*, U.S. Dept. of Commerce, National Bureau of Standards, 1978.

141 S. Sugano, *Multiplets of Transition-Metal Ions in Crystals*, Elsevier Science, 2012.

142 M. J. Freiser, S. Methfess and F. Holtzber, *Journal of Applied Physics*, 1968, **39**, 900–902.

143 A. Meijerink and G. Blasse, *Journal of Luminescence*, 1989, **43**, 283–289.

144 J. E. Van Haecke, P. F. Smet and D. Poelman, *Journal of Luminescence*, 2007, **126**, 508–514.

145 M. Suta, P. Larsen, F. Lavoie-Cardinal and C. Wickleder, *Journal of Luminescence*, 2014, **149**, 35–44.

146 S. J. Camardello, P. J. Toscano, M. G. Brik and A. M. Srivastava, *Journal of Luminescence*, 2014, **151**, 256–260.

147 H. A. Weakliem, *Physical Review B*, 1972, **6**, 2743–2748.

148 A. Yanase and T. Kasuya, *Progress of Theoretical Physics*, 1970, **46**, 388–410.

149 C. K. Duan and M. F. Reid, *Journal of Solid State Chemistry*, 2003, **171**, 299–303.

150 C. K. Duan, M. F. Reid and G. Ruan, *Current Applied Physics*, 2006, **6**, 359–362.

151 J. Torrent and V. BarrÃşn, in *Diffuse Reflectance Spectroscopy*, ed. A. Ulery and L. Drees, Soil Science Society of America, 2008, book section 13.

152 P. F. Smet, N. Avci, B. Loos, J. E. Van Haecke and D. Poelman, *Journal of Physics-Condensed Matter*, 2007, **19**, 246223.

153 T. Akai, M. Shigeiwa, K. Okamoto, Y. Shimomura, N. Kijima and T. Honma, *X-Ray Absorption Fine Structure-XAFS13*, 2007, **882**, 389–391.

154 A. B. Parmentier, P. F. Smet, F. Bertram, J. Christen and D. Poelman, *Journal of Physics D-Applied Physics*, 2010, **43**, 085401.

155 K. Korthout, A. B. Parmentier, P. F. Smet and D. Poelman, *Physical Chemistry Chemical Physics*, 2013, **15**, 8678–8683.

156 A. Parmentier, P. Smet and D. Poelman, *Materials*, 2013, **6**, 3663–3675.

157 A. Baran, S. Mahlik, M. Grinberg, P. Cai, S. I. Kim and H. J. Seo, *Journal of Physics-Condensed Matter*, 2014, **26**, 385401.

158 A. Lazarowska, S. Mahlik, M. Grinberg, C.-W. Yeh and R.-S. Liu, *Optical Materials*, 2014, **37**, 734–739.

159 D. D. Jia, *Journal of Luminescence*, 2006, **117**, 170–178.

160 M. M. Yuta and W. B. White, *Journal of the Electrochemical Society*, 1992, **139**, 2347–2352.

161 B. G. Tagiev, G. G. Guseinov, R. B. Dzhabbarov, O. B. Tagiev, N. N. Musaeva and A. N. Georgobiani, *Inorganic Materials*, 2000, **36**, 1189–1191.

162 C. Wickleder, S. Zhang and H. Haeuseler, *Zeitschrift Fur Kristallographie*, 2005, **220**, 277–280.

163 J. W. Kim and Y. J. Kim, *Journal of the European Ceramic Society*, 2007, **27**, 3667–3670.

164 R. Yu, R. X. Luan, C. F. Wang, J. T. Chen, Z. X. Wang, B. K. Moon and J. H. Jeong, *Journal of the Electrochemical Society*,

2012, **159**, J188–J192.
165 Y. K. Jeong, D. H. Cho, K. B. Kim and J. G. Kang, *Bulletin of the Korean Chemical Society*, 2012, **33**, 2523–2528.
166 J. J. Joos, K. Korthout, S. Nikitenko, D. Poelman and P. F. Smet, *Opt. Mater. Express*, 2013, **3**, 1338–1350.
167 B. Ordejon, L. Seijo and Z. Barandiaran, *Journal of Chemical Physics*, 2007, **126**, 194712.
168 M. G. Brik, *Journal of Alloys and Compounds*, 2008, **454**, 38–45.
169 P. S. Peijzel, A. Meijerink, R. T. Wegh, M. F. Reid and G. W. Burdick, *Journal of Solid State Chemistry*, 2005, **178**, 448–453.
170 E. G. Rogers and P. Dorenbos, *Journal of Luminescence*, 2014, **153**, 40–45.
171 E. G. Rogers and P. Dorenbos, *Journal of Luminescence*, 2014, **155**, 135–140.
172 E. G. Rogers and P. Dorenbos, *Ecs Journal of Solid State Science and Technology*, 2014, **3**, R173–R184.
173 B. Eisenmann, M. Jakowski, W. Klee and H. Schafer, *Revue De Chimie Minerale*, 1983, **20**, 255–263.
174 C. F. Guo, Q. Tang, D. X. Huang, C. X. Zhang and Q. A. Su, *Materials Research Bulletin*, 2007, **42**, 2032–2039.
175 C. F. Guo, Q. Tang, C. X. Zhang, D. X. Huang and Q. Su, *Journal of Luminescence*, 2007, **126**, 333–338.
176 C. Hidaka and T. Takizawa, *physica status solidi (c)*, 2013, **10**, 1123–1126.